Building on Oldroyd's viscoplastic legacy: Perspectives and new developments

N.J. Balmforth [a], R.V. Craster [b], D.R. Hewitt [c],*

[a] Department of Mathematics, University of British Columbia, Vancouver, BC, V6T 1Z2, Canada
[b] Departments of Mathematics & Mechanical Engineering, Imperial College, London SW7 2AZ, UK
[c] Department of Mathematics, University College, London WC1H 0AY, UK

A B S T R A C T

The decade following the second world war heralded the publication of a collection of important papers on non-Newtonian fluid mechanics; Oldroyd's work featured heavily in this collection. Not only did these articles establish important results, but Oldroyd's style and methods set the scene for subsequent work in the area, exploiting mathematical analysis to formulate problems, establish results and guide further research. While Oldroyd's name will forever be linked with the study of elastic fluids, the purpose of the present paper is to offer a modern perspective on a number of Oldroyd's papers on viscoplastic fluids from 1947–1951 [1–8]. Along the way, we sprinkle in a brief review of some of the subsequent developments stemming from Oldroyd's advances, together with a few new results guided by his work. Following the approach of most of Oldroyd's original papers, we focus on unidirectional flow down conduits. In an Appendix, we complement this discussion with a lubrication analysis, extending, clarifying and correcting the important original analysis of Walton and Bittleston (1991) [9]; although lubrication theory was not directly utilized by Oldroyd, the methodology aligns with his philosophy of using asymptotic and analytical approaches.

1. Oldroyd's eight viscoplastic papers

1.1. 'A rational formulation' [1]

The first of Oldroyd's forays into viscoplasticity resulted in his seminal paper on a 'rational formulation of the equations of plastic flow for a Bingham solid' [1]. In this paper, following the tensorial formulation of continuum mechanics, Oldroyd takes Bingham's concept of a material that can 'support finite stress elastically without flow and which flows ... when the stresses are sufficiently great' and determines the now well-known three-dimensional Bingham constitutive law. The paper has been widely cited and provides a definitive formulation of this tensorial law, which forms the basis of any modern study of viscoplastic fluids in more than one dimension.

Oldroyd begins armed only with the assumptions that the yield condition depends on the deviatoric components of the stress alone, the plastic viscosity μ_p above yield is constant, and the material is isotropic. He thus writes down a general rheological law for the deviatoric stress τ_{ij} above yield,

$$\tau_{ij} = \theta_{ij} + 2\mu_p \dot{\gamma}_{ij}, \tag{1}$$

in terms of a traceless yield-stress tensor θ_{ij} and (deviatoric) strain rate $\dot{\gamma}_{ij}$. Yield occurs when $\dot{\gamma}_{ij} = 0$. A series of geometrical arguments allow him to argue that the principal directions of θ_{ij}, τ_{ij} and $\dot{\gamma}_{ij}$ all coincide, and therefore that these three tensors are in proportion to one another.

Last, being the only permitted tensor-invariant form that is independent of the pressure, Oldroyd applies the von Mises criterion for yield,

$$\sqrt{\frac{1}{2}\sum_{i,j}\tau_{ij}\tau_{ij}} \equiv \tau = \tau_Y, \tag{2}$$

for some positive constant 'yield stress' τ_Y. Hence

$$\theta_{ij} = \frac{\tau_Y}{\tau}\tau_{ij}, \tag{3}$$

and we arrive at the Bingham law,

$$\tau_{ij} = \left(2\mu_p + \frac{\tau_Y}{\dot{\gamma}}\right)\dot{\gamma}_{ij} \quad \text{if} \quad \tau \geqslant \tau_Y, \tag{4}$$

where $\dot{\gamma}^2 = \frac{1}{2}\sum_{i,j}\dot{\gamma}_{ij}\dot{\gamma}_{ij}$. Below the yield stress, Oldroyd complemented (4) with a linearly elastic rheological law, accounting for solid-like deformation. Most modern statements of the Bingham law instead neglect any elastic deformation below yield, and complete the constitutive model by demanding $\dot{\gamma}_{ij} = 0$ when $\tau < \tau_Y$.

Armed with the tensorial Bingham law, Oldroyd continues on to discuss the energetics of a yield-stress material, establishing a minimum dissipation theorem for the flow of Bingham fluids. Prager [10] also derives this principle, whilst also establishing the maximum principal for the stresses and connections with analogous results from plasticity theory: together [1,10] lay key foundations for variational formulations of viscoplastic fluid mechanics.

---

* Corresponding author.
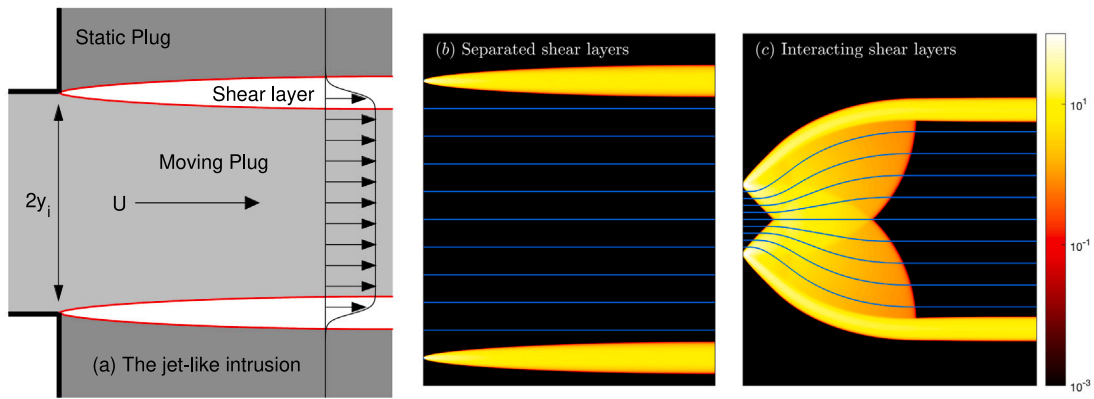 *E-mail address:* d.hewitt@ucl.ac.uk (D.R. Hewitt).

Fig. 1. (a) A sketch of Oldroyd's jet problem. In (b) and (c) we show numerical solutions for $Bi \gg 1$ (here $Bi = 2048$) adapted from [11] with different jet widths ($y_i = 1/2, 1/8$ respectively) that illustrate the two possible scenarios. The density map shows $\log_{10} \dot{\gamma}$ and blue contours show sample streamlines.

Oldroyd's paper arrived during the period that plasticity theory was being shaped into the form that we currently recognize, with the now-classical texts by Hill [12] and Prager & Hodge [13] emerging roughly contemporaneously. In fact, Prager and co-workers established the three-dimensional formulation of the Bingham law somewhat earlier than Oldroyd, taking a perspective much closer to solid mechanics and plasticity theory [14,15]. None the less, the approach of Oldroyd [1], and its rheological setting, marks the start of fluid viscoplasticity as we know it today. It is clear though that Oldroyd still viewed viscoplastic materials as 'Bingham solids' – that is, elastic solids that can undergo plastic flow for large enough stress – rather than the more standard modern view of 'Bingham fluids' that flow like a viscous fluid for large enough stress and remain essentially undeformed otherwise. Oldroyd's explicit allowance of the material to deform elastically below yield illustrated this viewpoint, which has resurfaced on a number of occasions (*e.g.* [16]) but has only relatively recently regained traction in modern viscoplastic modelling [17].

1.2. 'A plastic boundary-layer theory' [2]

Oldroyd's second paper outlines a plastic boundary-layer theory for a two-dimensional Bingham fluid motivated by the classical Blasius analysis of a boundary layer for a viscous Newtonian fluid. The theory predicts that the usual viscous shear stress across the boundary layer can be combined with contributions from the yield stress to balance pressure gradients down the layer. A characteristic thickness for the boundary layer emerges that scales as $Bi^{-\frac{1}{3}}$, where

$$Bi = \frac{\tau_Y L}{\mu_p U} \qquad (5)$$

is the Bingham number. Here, L and U are typical length and velocity scales in the flow direction. The theory is mapped out for $Bi \gg 1$, corresponding to the yield stress being much greater than typical viscous stresses.

Oldroyd's boundary-layer equation is rather more daunting than that in Blasius theory, amounting to a nonlinear partial differential equation for the streamfunction or velocity along the layer. However, Oldroyd went on to show that the equation admitted a self-similar solution corresponding to a thickening boundary layer that bridged between either two plugs, two regions of almost perfectly plastic deformation, or a combination of the two. That is, a free viscoplastic shear layer.

Oldroyd's analysis runs into difficulties when the boundary layer buffers a wall, being unable to satisfy all the boundary conditions and the continuity equation. Oldroyd felt that this indicated that elastic stresses needed to be included to save the situation. However, the analysis of exact unidirectional flow solutions, such as Oldroyd's for viscoplastic flow between coaxial cylinders [3] (his equations (7)-(8)),
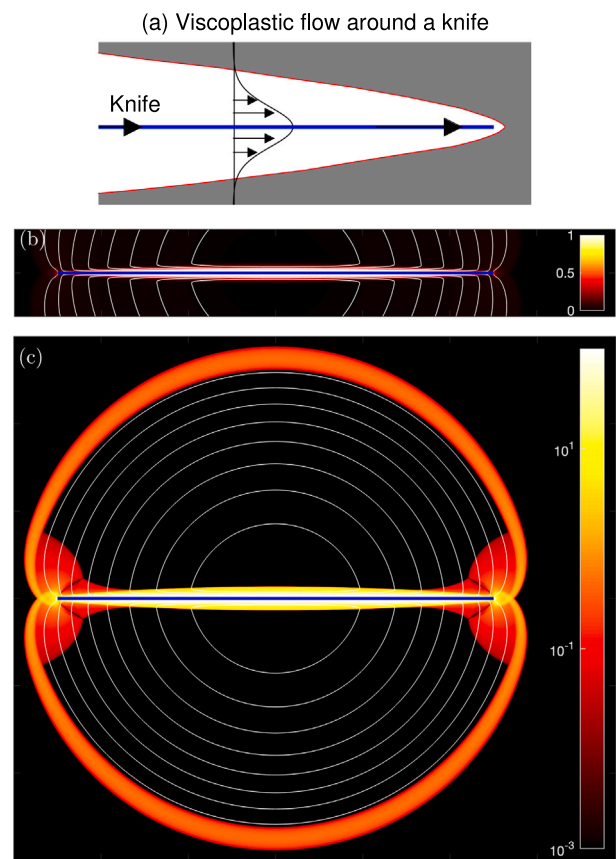

Fig. 2. (a) A sketch of Oldroyd's knife problem. In (b) and (c) we show a numerical solution adapted from [11] with $Bi = 512$; (b) shows the flow speed in the boundary layer against the knife, and (c) shows the logarithm of the strain rate over a wider region around the knife. Sample (white) streamlines are included in both panels.

or down a circular pipe [6] (his equation (57)), suggest that, in such cases, the boundary scalings may take a different form. Indeed, it turns out that boundary layers in a Bingham fluid against a rigid wall are typically characterized by a thickness of order $Bi^{-\frac{1}{2}}$ [11,18], and involve a rather simpler balance between viscous stresses and pressure gradients, with plastic terms playing no role.

Oldroyd suggested two canonical problems to explore in order to illustrate his boundary-layer theory: plastic flow around a moving knife and a plastic jet emerging from an orifice in a plane wall. These examples have indeed been found by [11] to possess boundary

layers with Oldroyd's self-similar structure; see Figs. 1 and 2. The first figure shows the boundary-layer structure developing at the edges of a viscoplastic jet. Although Oldroyd's prediction is borne out by numerical simulations (as reproduced in Fig. 1), his construction is not the complete story: if the width of the jet is too small, the boundary layers interact and a more complicated pattern of nearly perfectly plastic flow develops across the orifice; the jet thereby expands before settling into Oldroyd's pattern (see [11] for further details).

Oldroyd's second example is the viscoplastic flow around a translating, two-dimensional plate, or "knife" (Fig. 2), a configuration that has motivated a number of experiments [19–21]. However, Oldroyd's theory does not, in fact, apply to the boundary layers against the side of the knife, as pointed out by Piau [18,22]; these layers instead have a $\mathrm{Bi}^{-\frac{1}{2}}$ scaling for Bingham fluid (or $\mathrm{Bi}^{-\frac{1}{n+1}}$ for Herschel–Bulkley fluid). Nevertheless, the example provides a convenient illustration of this latter type of boundary layer, as illustrated by the numerical example also shown in Fig. 2. This computation uses a plate of finite length instead of the half-plane introduced by Oldroyd. Again there are some surprises: most notably, the boundary layers against the plate are not the only regions of flow. Instead a complicated zone of nearly perfectly plastic deformation also arises at the front and back of the plate as well as an extensive rotating plug. Moreover, the free shear layers that border the rotating plug *are* described by Oldroyd's boundary-layer theory. Oldroyd's theory does therefore apply to the knife problem, but not as in Oldroyd's original vision. Larger-scale deformation of this form away from the plate has also been observed experimentally [20] and found theoretically for flows around ellipses with high aspect ratio [23].

We revisit Oldroyd's boundary layer theory and canonical examples below in a variation of the two-dimensional viscoplastic flow problem. In particular, we consider steady unidirectional flow down a conduit of arbitrary cross-section. This second type of viscoplastic flow problem is the subject of the third and fourth series of Oldroyd's papers, discussed in the next subsections, and has received much wider attention in view of various industrial applications. In the limit of a strong yield stress, or close to the onset of flow, the conduit flow also develops the two types of viscoplastic boundary layers, and Oldroyd's canonical examples again provide useful illustrations. One important difference between the 2D and conduit problems, however, is that the constraints that make Oldroyd's theory problematic for a boundary layer against a wall do not feature in the latter. As a result, as we will find below, one can find $\mathrm{Bi}^{-\frac{1}{3}}$ layers against the wall of a conduit.

1.3. 'Conduit flow' [3–6]

In this series of papers, Oldroyd constructs solutions for the unidirectional flow of Bingham fluid down a conduit with a variety of geometries. In many ways, the papers set the stage for later work on viscoplastic flow down conduits of arbitrary cross section (*e.g.* [9,24–32]).

The first two papers discuss flow between two boundaries in relative motion, taking eccentric circles or confocal ellipses as illustrative wall shapes. For eccentric circular cylinders [3], Oldroyd's strategy is to build solutions perturbatively, using the yield stress as the expansion parameter and exploiting complex-variable techniques (conformal mapping) to ease the algebraic construction. Although this strategy limits the solutions to being yielded throughout the domain, it did furnish helpful solutions in an age before the widespread availability of computing power. However, Oldroyd also makes the important general point that once a boundary becomes fully plugged up, its precise shape and location become irrelevant to the velocity solution. The "cloaked" wall impacts merely the stress distribution within the plug, thereby influencing the conditions for which the plug breaks to "uncloak" that boundary, but otherwise remains irrelevant. The flow in the yielded region conforms only to the shape of an unplugged boundary, including inheriting its symmetries (even when the other boundary has other

symmetries). Consequently, for an eccentric annulus, the inner yielded region becomes axisymmetric about the centre of the inner circle once the outer circle becomes hidden within a plug. Oldroyd was then able to construct solutions with higher yield stress (where the outer boundary is likely to plug up) without knowing precisely for what range of τ_Y these might arise.

In [4], Oldroyd repeats the perturbation expansion for boundaries with the form of confocal ellipses. Again, the solutions are limited to the fully yielded regime, with a plugged outer ellipse expected at high yield stress. This time, however, the elliptical geometry precludes a straightforward solution for the latter states. Instead, Oldroyd invents an iterative technique to converge to the correct solution: he uses the solution for flow between two walls to approximate that between a wall and a yield surface. Then, by a clever construction, he refines this approximation to correct the yield surface position, in a manner that could be applied repeatedly for successive improvements.

Oldroyd's point about cloaking is widely exploited in viscoplastic fluid mechanics nowadays (*e.g.* [33,34]). It applies in other conduit flows when a plug intervenes between the two boundaries, isolating separate yielded regions. In this case, each sheared zone is affected only by the shape of adjacent boundary, and independent of the other one. The asymmetries between the boundary shapes is therefore entirely accounted for by the plug. This result underscores a construction by Szabo & Hassager [25] that we return to in Section 4.2 for eccentric annuli, and how solutions for flow in certain geometries lead to solutions in other conduits (see Sections 3.1 and 3.2).

Oldroyd's third paper in this series on conduit flow digresses further into the differential geometry underlying the problem, considering more general bounding surfaces, assuming only that the velocity contours (and therefore walls and plugs) are coordinate lines of some orthogonal coordinate system. Ultimately he chooses a plane wall and a wall shaped like a catenary to arrive at an exact solution for the flow of a Bingham fluid within a relatively complicated geometry (see Section 3.2).

The fourth paper [6] takes a somewhat different tack, considering unsteady problems. Oldroyd first establishes an equation of motion for the yield surface, and draws an analogy with a certain kind of Stefan problem. Eventually, he settles on flows within a uniform conduit driven time-dependently either by the relative motion of the walls, a pressure gradient, or both. This type of flow problem has been explored further in [35–38], where methods developed for Stefan problems are used to attack the problem, or analysis for early times establishes how the yield surface is set into motion. By contrast, Oldroyd builds an analytical similarity solution for a uniformly accelerating boundary. Subsequent developments in this vein have considered oscillating flows in which multiple plugs can appear [39–42].

1.4. 'Beyond Bingham' [7,8]

In the last two papers [7,8], Oldroyd advances beyond the Bingham model, considering constitutive laws with general nonlinear plastic viscosity functions. Paper [7] addresses the generalization of the differential geometry in [5] to such fluids, offering a generalization of the catenary solution for a particular viscosity function.

Finally, Oldroyd takes a different approach in [8] to tackle rectilinear flows, without a driving pressure gradient, by using a hodograph transform to convert the nonlinear partial differential equation for the velocity into a linear one for a conjugate variable that depends on the shear-rate components, now considered independent variables. This permits Oldroyd to build some special exact solutions corresponding to flow past a nearly elliptical obstruction for two specific model fluids. Oldroyd's analysis is closely related to similar approaches in nonlinear filtration theory, as observed by Entov [43]. Entov further exploited the correspondence to propose additional exact solutions for viscoplastic flow. More exact solutions using the hodograph technique are given in [44–48] for Bingham and Herschel–Bulkley fluids.

Section 2.4 provides a brief summary of the hodograph approach. Importantly, although they strictly apply to highly specific geometries, certain solutions of the hodograph problem apply quite generally whenever the yield stress becomes relatively small. More specifically, the hodograph solutions provide the leading order form of a more general solution within the small or remote regions where the strain rates are low. Thus, the hodograph approach can be exploited to build approximate yield surfaces. We exploit these features in Sections 2 and 4, to provide expressions for the shape of the yield surfaces around Oldroyd's knife and in the corners of square ducts.

In [7,8], Oldroyd's main (analytical) results are established for certain non-standard nonlinear viscosity functions, owing to the need to solve the equation on the hodograph plane (which simplifies for those viscosity functions). Nowadays, such an approach may well be viewed with some caution in view of the familiar and simple appeal of the mathematical form of the Bingham and Herschel–Bulkley laws. However, Oldroyd's point was that such analytically simple choices may not be either suitable for a real fluid with a complicated rate-dependent viscosity, or easy to work with to find exact solutions. Oldroyd presents an alternative strategy wherein we adjust the constitutive law to ease the analysis, with alternative choices perhaps being just as straightforward to fit to a flow curve. Though unconventional for viscoplastic flows, this perspective has been exploited with modified Darcy laws in filtration theory and viscoplastic flows in Hele-Shaw cells (*e.g.* [49–56]).

In retrospect, all but the first two of Oldroyd's eight papers have received little citation, other than as examples of approximate solutions for flows in more complicated or specific geometries. Nevertheless, all eight papers were clearly seminal, advocating the use of applied mathematical techniques to study complex fluid flows. Oldroyd's particular emphasis on locating and tracking yield surfaces foreshadowed many of the concerns in later literature. It is not unreasonable to suppose that the insights and tools set out by Oldroyd are undervalued and might still provide traction in the future.

2. Steady conduit flow

We illustrate in more detail a number of Oldroyd's advances by considering the special example of uni-directional viscoplastic flow down a conduit. More specifically, we consider a Herschel–Bulkley fluid moving down a conduit with an arbitrarily shaped, but fixed cross-section, driven either by a pressure gradient or the differential motion of the walls. Our formulation of the problem mimics Oldroyd's; some of the developments either follow subsequent work or establish new results, but in all cases, we are guided by Oldroyd's hand.

2.1. Formulation and preliminary observations

If the conduit has a characteristic lengthscale L, and the flow a typical speed V, then we may cast the problem in a dimensionless form by scaling lengths and speed by these measures. For a Herschel–Bulkley fluid, the problem to be solved for the flow speed $w(x, y)$ over the yielded regions is then

$$\boldsymbol{\nabla} \cdot (\dot{\gamma}^{n-1}\boldsymbol{\nabla}w) + \mathrm{Bi}\boldsymbol{\nabla} \cdot \left(\frac{\boldsymbol{\nabla}w}{\dot{\gamma}}\right) + Y = 0, \tag{6}$$

$$\dot{\gamma} \equiv |\nabla w| \equiv \sqrt{\left(\frac{\partial w}{\partial x}\right)^2 + \left(\frac{\partial w}{\partial y}\right)^2}, \tag{7}$$

where

$$\mathrm{Bi} = \frac{\tau_{\mathrm{Y}}}{K}\left(\frac{L}{V}\right)^n \tag{8}$$

is the Bingham number. Here, Y is the magnitude of the dimensionless pressure gradient, the dimensional gradient being scaled by $K(V/L)^n/L$ and assumed either zero or negative to drive flow in the positive z−direction. In practice, if the motion of one of the walls drives fluid

flow, then we choose V as the speed of that boundary; if the walls are not in motion and a pressure gradient drives flow, then V can be chosen to set Y to unity.

In addition to yielded zones, the conduit may contain rigid plugs. At the yield surfaces that separate the two regions, we must impose $\dot{\gamma} \equiv |\nabla w| = 0$. A plug that is attached to one of the walls must move at the speed of that boundary, but there may also be embedded plugs with speed $w = w_p$. As discussed by Oldroyd [6], the force balance on an embedded plug demands that

$$YA = \pm\ell\mathrm{Bi}, \tag{9}$$

where A is the area of the plug, ℓ is the length of its perimeter and we select the sign according to whether the plug advances past either slower (+) or faster (−) fluid everywhere just beyond the yield surface. A generalization of this condition to the situation that the plug moves faster than the surrounding fluid over part of its periphery (of length ℓ_+), and slower over the remainder (of length ℓ_-) is as follows. Approaching the plug, the shear stress reduces to

$$\mathrm{Bi}\frac{\nabla w}{|\nabla w|} \equiv \mathrm{Bi}\,\hat{\mathbf{n}} \tag{10}$$

(as noted by Oldroyd [6]), where $\hat{\mathbf{n}}$ is the unit vector normal to the curve of constant w (in this case, the yield surface) in the direction of increasing w. Integrating (6) over the area of the plug and using Gauss's theorem then furnishes

$$YA = \mathrm{Bi}(\ell_+ - \ell_-). \tag{11}$$

For the conduit problem, Oldroyd's (and Prager's) energy equation follows from multiplying (6) by w and integrating over a domain Ω with boundary $\partial\Omega$. After some manipulations again involving Gauss's theorem, we find

$$\iint_{\Omega} wY\mathrm{d}x\mathrm{d}y \equiv YQ = \iint_{\Omega} \tau\dot{\gamma}\mathrm{d}x\mathrm{d}y - \oint \left[w(\tau_{xz}, \tau_{yz})\right]_{\partial\Omega} \cdot \hat{\mathbf{n}}_{\Omega}\mathrm{d}s, \tag{12}$$

where Q is the flux across Ω, and $\hat{\mathbf{n}}_{\Omega}$ and s are the outward normal and arc length of $\partial\Omega$. The physical content of this mathematical statement is that the power demanded of the pressure gradient to drive the fluid through Ω is equal to the dissipation rate by the viscous and plastic stresses, less the power input by the forces acting on $\partial\Omega$.

As a final initial preparation, we note that, in curvilinear coordinates (ς, η), in which ς denotes arc length along some curve and $\epsilon\eta$ is the transverse coordinate, the governing equation can be written as

$$\frac{1}{h}\left(\frac{\mu}{h}w_{\varsigma}\right)_{\varsigma} + \frac{1}{\epsilon^2}\left(\mu w_{\eta}\right)_{\eta} - \frac{\kappa\mu}{\epsilon h}w_{\eta} = -Y, \tag{13}$$

where

$$\mu(\dot{\gamma}) = \dot{\gamma}^{n-1} + \frac{\mathrm{Bi}}{\dot{\gamma}}, \qquad h = 1 - \epsilon\eta\kappa, \qquad \dot{\gamma} = \sqrt{\frac{w_{\varsigma}^2}{h^2} + \frac{w_{\eta}^2}{\epsilon^2}} \tag{14}$$

and κ is the local curvature. Note that, in these relations, we have introduced a shorthand, subscript notation for derivatives of w with respect to ς and η, and a scaling $\epsilon \ll 1$ for the transverse coordinate that we will exploit in performing boundary-layer theory.

2.2. Perfectly plastic deformation and the yield surfaces

When the yield stress dominates the stress one expects that the fluid must deform like a perfectly plastic fluid everywhere it is yielded, except over thin boundary layers where viscosity remains important. Here, we access this limit by taking $\mathrm{Bi} \gg 1$, assuming that the velocity scale V can be prescribed. For pressure-driven flow, in which the driving gradient is given and we scale Y to unity, typical speeds are unknown and the plastic limit corresponds to the initiation of flow with $w \ll 1$.

To expose the plastic limit more clearly, we follow Oldroyd [6] and take the curve $\eta = 0$ to be a contour of constant velocity with $w_\eta > 0$ in (13)–(14). Then,

$$\frac{1}{\epsilon}\frac{\partial \tau_{\eta z}}{\partial \eta} - \frac{\kappa}{h}\tau_{\eta z} = -Y, \quad \tau_{\eta z} \equiv \frac{\mu}{\epsilon} w_\eta = \left(\frac{w_\eta}{\epsilon}\right)^n + \text{Bi}. \quad (15)$$

For a region of almost perfectly plastic deformation, we take $\text{Bi} \gg 1$ and $\epsilon = O(1)$. We then set $\tau_{\eta z} = \text{Bi}$ to arrive at

$$\kappa \text{Bi} = Y, \quad (16)$$

for the constant speed contour $\eta = 0$. Evidently, Y must be $O(\text{Bi})$ in order to drive motion (*cf.* (9)). Since that pressure gradient is also constant, (16) demands that the contours of constant w must all be circular arcs of the same radius. This is clearly impossible if the region of perfectly plastic deformation has finite area. Thus, there cannot be any such regions, in contrast to two-dimensional viscoplastic flow, where they may appear, threaded by the sliplines of plasticity theory (the characteristics of the stress field) [12,13].

For $\text{Bi} \to \infty$, the conduit flow must therefore become confined to viscoplastic boundary layers separating plugs from one another and the walls. Over these boundary layers, we take ϵ to be sufficiently small to promote the importance of the viscous stress. If $1 \ll \epsilon^{-n-1} \ll \text{Bi}$, however, we still cannot escape the constraint in (16), which demands that the boundary layer is a circular arc; only when $\epsilon^{-n-1} \sim \text{Bi}$ can the boundary layer follow a different curve. As we argue next, this dichotomy leads to two types of boundary layers. In particular, when the boundary layer is sandwiched between yield surfaces that lie away from the walls, this "free shear layer" must be circular (as has been established more formally [24,29]); in this case, Oldroyd's boundary-layer theory [2] applies, as discussed below in Section 2.3.2. First, however, we discuss the other situation, where the boundary layer lies against a wall and adopts the shape of that boundary.

2.3. Plastic boundary-layer theory

2.3.1. Viscoplastic boundary layers against a wall (a.k.a. between a plug and a hard place)

For a boundary layer that lies against a wall moving with speed w_b, we use that boundary to locate the curve $\eta = 0$ in (13), and there let $w = w_b$. At the other side of the boundary layer, the viscous influence must disappear to leave either a region of perfectly plastic deformation or a plug. But the arguments above indicate that there can be none of the former regions. Thus, we set $w = w_p$ and $w_\eta = 0$ at the yield surface, $\eta = Y(\varsigma)$, that borders the boundary layer at the other side.

In this setting, we now draw a parallel with the theory for $\text{Bi}^{-\frac{1}{2}}$ layers in the 2D flow problem. For this task, we first observe that the pressure gradient, if responsible for flow, must be sufficient to drive the fluid past the wall and counter the resisting viscous stress, leading us to set $Y = \epsilon^{-n-1}Y_{n+1}$. If we further take $\epsilon = \text{Bi}^{-\frac{1}{n+1}}$, then $Y = O(\text{Bi})$, as demanded by force balance on the plug in (9) or (11). The leading-order boundary-layer equation is then

$$(|w_\eta|^{n-1} w_\eta)_\eta \sim \sigma\kappa - Y_{n+1}, \quad (17)$$

where $\sigma = \text{sgn}(w_\eta) \equiv \text{sgn}(w_p - w_b)$. Hence

$$w = w_b + (w_p - w_b)\left[1 - \left(1 - \frac{\eta}{Y}\right)^{1+\frac{1}{n}}\right], \quad (18)$$

and

$$w_p = w_b - \frac{nY^{1+\frac{1}{n}}}{n+1}|\sigma\kappa - Y_{n+1}|^{\frac{1}{n}}\,\text{sgn}(\sigma\kappa - Y_{n+1}). \quad (19)$$

Evidently, this theory can only apply provided

$$Y \equiv \text{Bi}Y_{n+1} \neq \sigma\kappa\text{Bi}. \quad (20)$$

In particular, the theory fails when there is no pressure gradient and the wall is straight ($Y_{n+1} = \kappa = 0$).

2.3.2. Free viscoplastic shear layers

We may find the analogue of Oldroyd's $\text{Bi}^{-\frac{1}{3}}$ layer for a free shear layer centred at $\eta = 0$, or when the theory of Section 2.3.1 fails for a wall located at $\eta = 0$: working with the left-hand side of (13), we first observe that the leading order term, for $\text{Bi} \gg 1$ and $\epsilon \ll 1$, is $\epsilon^{-2}\text{Bi}(\dot\gamma^{-1}w_\eta)_\eta$. But since $\dot\gamma \sim |w_\eta|$, this term vanishes identically. The next term to appear arises from the third term on the left of (13), and is $-\kappa\text{Bi}\sigma$. This must be balanced by the leading-order of the right-hand side, and so $Y \sim \kappa\text{Bi}\sigma$. This condition reinforces the idea that the centreline of a free shear layer must follow a circular arc, or that the theory of Section 2.3.1 fails when (20) is violated.

The next corrections to the left-hand side of (13), constitute the two combinations,

$$\epsilon^{-n-1}(|w_\eta|^{n-1}w_\eta)_\eta \quad (21)$$

and

$$\epsilon\sigma\text{Bi}\left[\left(\frac{w_\varsigma}{w_\eta}\right)_\varsigma - \left(\frac{w_\varsigma^2}{2w_\eta^2}\right)_\eta + \eta\kappa\right], \quad (22)$$

where $\sigma = \text{sgn}(w_\eta)$. Assuming both are in balance, we find $\epsilon = \text{Bi}^{-\frac{1}{n+2}}$. With $Y = \kappa\text{Bi}\sigma + \epsilon^{-n-1}Y_{n+1}$, we then arrive at Oldroyd's boundary-layer equation,

$$(|w_\eta|^{n-1}w_\eta)_\eta + \sigma\left[\left(\frac{w_\varsigma}{w_\eta}\right)_\varsigma - \left(\frac{w_\varsigma^2}{2w_\eta^2}\right)_\eta\right] = -Y_{n+1} - \eta\sigma\kappa, \quad (23)$$

except for some differences in the numerical values of some of the coefficients, and that the pressure gradient here is constant. For a free shear layer, this equation must be solved subject to the edge conditions,

$$w(\varsigma, Y_\pm) = W_\pm \quad \& \quad w_\eta(\varsigma, Y_\pm) = 0, \quad (24)$$

where $\eta = Y_\pm$ are the bordering yield surfaces where the plug have speeds $W_\pm$. Alternatively, for a wall layer, we may apply $w(\varsigma, 0) = w_b$, $w_\eta(Y_+) = 0$ and $w(\varsigma, Y_+) = w_p$.

For a free shear layer with $Y_{n+1} = \kappa = 0$, there is a self-similar solution to (23) and (24) of the form

$$w = \frac{1}{2}(W_- + W_+) + |W_+ - W_-|\, f(\zeta), \quad (25)$$

where

$$\zeta = -\frac{\sigma\eta}{Y(\varsigma)} \quad \& \quad Y_\pm = \pm Y(\varsigma), \quad (26)$$

as noticed by Oldroyd [2] in the Bingham case, and discussed more thoroughly in [11]. The half-width of the shear layer $Y(\varsigma)$ and the profile function $f(\zeta)$ satisfy

$$\frac{\text{d}^2 Y}{\text{d}\varsigma^2} = -\frac{\lambda|W_+ - W_-|^n}{Y^{n+1}} \quad \& \quad (|f_\zeta|^{n-1}f_\zeta)_\zeta = \lambda\zeta, \quad (27)$$

with a separation constant λ given by

$$\lambda = 2\left[\frac{n\Gamma(\frac{3}{2} + \frac{1}{n})}{\sqrt{\pi}\,\Gamma(\frac{1}{n})}\right]^n, \quad (28)$$

where $\Gamma(x)$ is the Gamma function. For a Bingham fluid, the solution is more explicit, with

$$f(\zeta) = \frac{1}{4}\zeta(\zeta^2 - 3), \quad \lambda = \frac{3}{2} \quad (29)$$

and

$$\tan^{-1}\sqrt{\frac{Y}{Y_E - Y}} - \frac{\sqrt{Y(Y_E - Y)}}{Y_E} = \frac{\varsigma\sqrt{3|W_+ - W_-|}}{Y_E^{\frac{3}{2}}}, \quad (30)$$

if $Y(0) = 0$ and $Y = Y_E$ at the position where $Y'(s) = 0$ (*cf.* [11]).

The self-similar solution also applies to a wall layer with $Y_{n+1} = \kappa = 0$, provided we take $W_- = 2w_b - w_p$, $W_+ = w_p$, $Y_- = -Y_+$ and $\eta > 0$. For conduit flow, this solution is acceptable because there are no further boundary conditions or constraints to impose. By contrast, in the 2D flow problem, the satisfaction of the continuity equation and the additional boundary conditions at the wall rule out Oldroyd's theory.

2.4. Hodograph transform

As noted earlier, Oldroyd [8] draws upon the hodograph approach, popular in gas-dynamics as Chaplygin's transformation, and which is a Legendre transformation. This approach is powerful in generating exact solutions to specific problems, but is less helpful in general settings. However, one aspect of the hodograph method does remain generally useful for conduit flows: when $\text{Bi} \ll 1$, canonical plug shapes emerge and these general shapes are ubiquitous. We briefly outline their origin for the Bingham fluid, *i.e.* $n = 1$.

The hodograph analysis [43–47,57] relies on a switch of the independent variables. This is achieved by setting $W(x, y) = \psi(\rho, \Theta)$ with $(w_x, w_y) = \text{Bi}\rho(\sin\Theta, -\cos\Theta)$, where $\rho = \text{Bi}^{-1}\dot{\gamma}$. Neglecting the pressure gradient Y, the governing equation (6) is then transformed into the linear problem,

$$\frac{\rho^2}{1+\rho} \frac{\partial}{\partial\rho}\left[\frac{(1+\rho)^2}{\rho}\frac{\partial\phi}{\partial\rho}\right] + \frac{\partial^2\phi}{\partial\Theta^2} = 0. \tag{31}$$

This is the crucial advantage of the hodograph approach: in (31) we now have a standard linear elliptic partial differential equation (PDE) to deal with rather than the awkward nonlinear PDE in (6). In particular, the limit as $\rho \to 0$ extracts the yield surface profile explicitly. Sadly the transformation back to the physical plane, which is accomplished by

$$dx + i\,dy = \frac{e^{i\Theta}}{\rho\text{Bi}}\left[\frac{\psi_\Theta d\rho}{\rho} - (1+\rho)\psi_\rho d\Theta - i\,d\psi\right], \tag{32}$$

is non-trivial for realistic problems and the methodology is of no direct advantage for pressure-gradient driven flows. Nevertheless, recognizing that there exist simple solutions to the linear PDE that characterize common local flows means that this hodograph approach can be usefully exploited.

Several simple solutions of (31) emerge by assuming separable solutions of the form

$$\psi(\rho, \Theta) = a_m(\rho)\sin\Phi \quad \& \quad \Phi = m\Theta + \phi, \tag{33}$$

where ϕ is an arbitrary phase that, along with m, must be selected to enforce boundary conditions [57]. An analysis of the differential equation satisfied by $a_m(\rho)$ indicates the limits, $a_m \sim \alpha_m A \rho^2$ for $\rho \to 0$ and $a_m \sim A\rho^m$ for $\rho \gg 1$.

Four important cases are given by $m = 0, 1, 2$ and $\frac{1}{2}$. The simplest hodograph solution, with $m = 0$, is

$$\psi = A\left(\log(1+\rho) - \frac{\rho}{1+\rho}\right) \to \begin{cases} \frac{1}{2}A\rho^2, & \rho \to 0, \\ A\log\rho, & \rho \to \infty, \end{cases} \tag{34}$$

and so $\alpha_0 = \frac{1}{2}$. For $m = 1$ and 2, we have the analytical solutions,

$$a_1(\rho) = A\rho^2/(1+\rho) \quad \& \quad a_2(\rho) = A\rho^2 \tag{35}$$

(implying $\alpha_1 = \alpha_2 = 1$); $a_{\frac{1}{2}}(\rho)$ is a special function [57] but can also be effortlessly constructed numerically. We note $\alpha_{\frac{1}{2}} \approx 0.5891$.

At the yield surface, $\rho \to 0$ and $d\rho = d\psi = 0$, giving

$$x + iy = x_* + iy_* + \frac{\alpha_m A}{\text{Bi}}\left[\frac{e^{i(\Theta+\Phi)}}{m+1} + \frac{e^{i(\Theta-\Phi)}}{m-1}\right], \tag{36}$$

for $m \neq 1$, and

$$x + iy = x_* + iy_* + \frac{A}{\text{Bi}}\left[\frac{1}{2}e^{i(\Theta+\Phi)} + i\Theta e^{i\phi}\right], \tag{37}$$

if $m = 1$, where x_* and y_* are integration constants. In the (Newtonian) "far-field", $\rho \gg 1$, we find

$$x + iy = X + iY + \frac{A}{\text{Bi}} \times \begin{cases} m(m-1)^{-1}\rho^{m-1}e^{i(\Theta-\Phi)}, & m \neq 1, \\ (\log\rho - i\Theta)e^{-i\phi}, & m = 1, \end{cases} \tag{38}$$

where X and Y are two further constants of integration. Consequently, the constant A must be identified by matching up the far-field solution $A\rho^m\sin\Phi$, with that solving the Newtonian problem in question, exploiting (38). The yield surface is then prescribed by (36) or (37).

2.4.1. Circular yield surfaces; $m = 0$

With $m = 0$, we transform back to the physical plane using

$$dx + i\,dy = -\frac{Ae^{i(\Theta+\frac{1}{2}\pi)}}{\text{Bi}(1+\rho)^2}d\rho. \tag{39}$$

The far-field ($\rho \gg 1$) solution is therefore $\psi \sim A\log(|A|r/\text{Bi})$, where r is the radial coordinate, and the yield surface is the circle $r = r_p = \text{Bi}^{-1}|A|$.

2.4.2. Corner flow; $m = 2$

For the $m = 2$ solution, with $\phi = 0$, $A = c\text{Bi}^2$ and $\psi = c\text{Bi}^2\rho^2\sin 2\Theta$, the transformation back to physical space is given by

$$x = x_* + c\text{Bi}(2\rho\cos\Theta + \frac{4}{3}\cos^3\Theta), \tag{40}$$

$$y = y_* - c\text{Bi}(2\rho\sin\Theta + \frac{4}{3}\sin^3\Theta) \tag{41}$$

The far-field solution therefore converges to the Newtonian stagnation-point flow,

$$w \sim -\frac{(x-x_*)(y-y_*)}{2c}, \tag{42}$$

centred at (x_*, y_*). Conversely, for $\rho \to 0$, we may extract the yield surface

$$(x-x_*)^{2/3} + (y-y_*)^{2/3} = (\frac{4}{3}c\text{Bi})^{2/3}. \tag{43}$$

Evidently, once c is chosen from a match in the far field, (43) provides a convenient parameterization of the yield surface, which has a scale of $O(\text{Bi})$. In Section 4.1, we demonstrate how (43) approximates the yield surfaces in the corners of a square duct for pressure-driven viscoplastic flow with a low yield stress (the pressure gradient being unimportant on the small scale of this feature).

2.4.3. Sinusoidal flow; $m = 1$

For $m = 1$, with $\phi = -\frac{1}{2}\pi$, the solution is

$$x = X + \frac{A}{\text{Bi}}\left(\Theta + \frac{\sin 2\Theta}{2(1+\rho)}\right), \tag{44}$$

$$y = Y + \frac{A}{\text{Bi}}\left[\log(1+\rho) - \frac{\cos^2\Theta}{1+\rho}\right], \tag{45}$$

$$\psi = \frac{A\rho^2}{1+\rho}\cos\Theta, \tag{46}$$

which gives the far-field sinusoidal form,

$$w(x, y) \sim Ae^{\frac{\text{Bi}}{A}(y-Y)}\cos\frac{\text{Bi}}{A}(x-X), \tag{47}$$

to be matched to the corresponding Newtonian solution for the problem in question (such as the example below in Section 3.1). Having determined A, X and Y thus, the corresponding yield surface follows from taking $\rho \to 0$,

$$x = 1 - \pi^{-1}(\sin 2\Theta + 2\Theta), \tag{48}$$

$$y = Y + 2\pi^{-1}\cos^2\Theta. \tag{49}$$

2.4.4. The dipole solution; $m = \frac{1}{2}$

With $m = \frac{1}{2}$ and $\phi = -\frac{1}{4}\pi$, we may find a fourth solution centred at the origin of the physical plane with the far-field form,

$$\left.\begin{array}{l} \psi \sim A\rho^{\frac{1}{2}}\sin\Phi, \\ x \sim A\text{Bi}^{-1}\rho^{-\frac{1}{2}}\sin\Phi, \\ y \sim -A\text{Bi}^{-1}\rho^{-\frac{1}{2}}\cos\Phi, \end{array}\right\} \to w \sim \frac{A^2x}{\text{Bi}(x^2+y^2)}, \tag{50}$$

where $\hat{\Theta} = \Theta + \frac{1}{4}\pi$. The corresponding yield surface is given parameterically by (36). This solution was referred to as a dipole in the 1960s Russian literature on nonlinear filtration [57], and describes the remote plug surrounding a moving section of a wall, as we discuss below in Section 3.1.

The yield surfaces implied by the three solutions outlined above for $m > 0$ are illustrated in Fig. 3. The solutions with other values for m correspond to flow through wedges of varying angle [45].
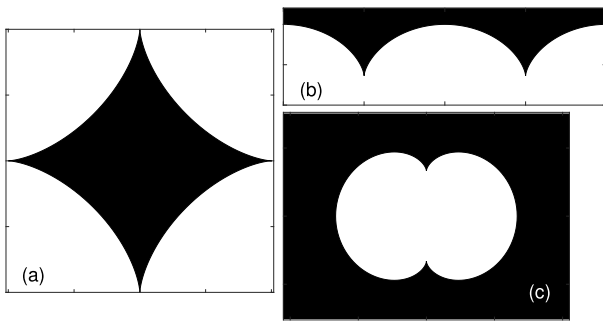
Fig. 3. The yield surfaces of the three hodograph solutions for (a) $m = 2$, (b) $m = 1$ and (c) $m = \frac{1}{2}$.
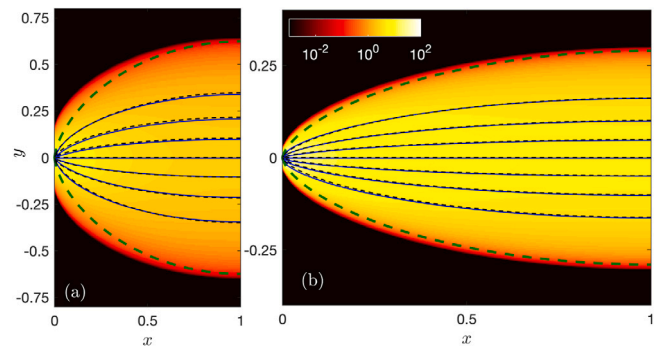

Fig. 4. Numerical and asymptotic solutions for sliding half-planes with (a) $Bi = 10$ and (b) $Bi = 100$. The figure shows a density map of $\log_{10} \dot{\gamma}$ for the numerical solution (with the colorbar indicated) and blue lines show corresponding contours of constant speed $w(x, y)$ spaced by increments of 0.25. The dashed lines show the yield surface (green) and speed contours (black) of the self-similar asymptotic solution. The domain has lengths $L_x = 1$ and $L_y = 2$ (not all the domain is shown).
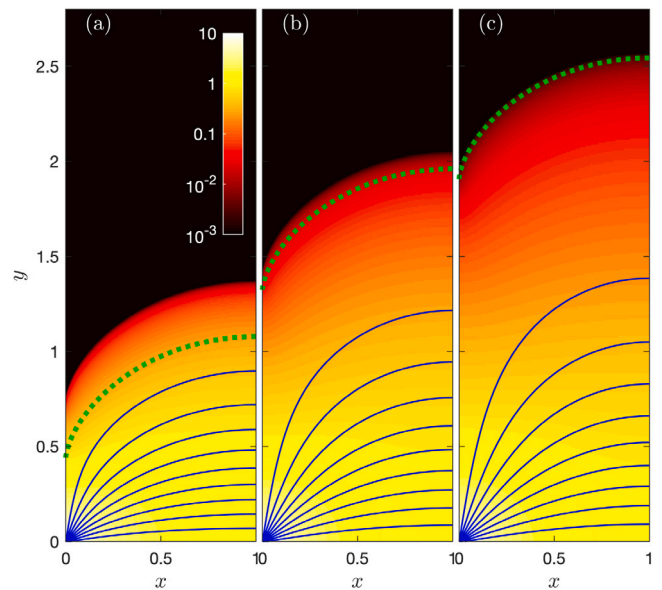
3. Wall-driven conduit flows

Inspired by Oldroyd's work and armed with the tools set out in Section 2, we now explore viscoplastic flows down conduits driven by the differential motion of the walls. In particular, we consider the analogues of two of Oldroyd's canonical problems [2], providing numerical solutions and examining the limits of high ($Bi \gg 1$) and low ($Bi \ll 1$) yield stress.

3.1. Sliding panels

The unidirectional analogue of Oldroyd's jet (Fig. 1) is the motion parallel to a wall driven by a sliding panel; *i.e.* a specific case of the class of flow problems in the half space $x > 0$ in which the velocity $w(0, y)$ is imposed. In particular, the jet corresponds to the flow driven by a panel of finite width that slides along the wall in the direction of its length, with the remainder of the wall locked in place.

Before attacking such sliding panels, we address a slightly simpler problem in which half the wall moves in one direction at speed V whilst the other half travels in the opposite direction with speed $-V$. The dimensionless boundary condition is

$$w(0, y) = \text{sgn}(y). \tag{51}$$

The 2D problem corresponding to this unidirectional flow problem is the one-sided intrusion discussed in [11] as a simplification of Oldroyd's jet, which features a single viscoplastic shear layer stemming from the velocity jump at $y = 0$.

Practically, we solve this problem numerically in a domain of finite size, $0 < x < L_x$ and $-L_y < y < L_y$, using an augmented Lagrangian scheme similar to that outlined in [48]. As long as L_y is sufficiently large, the precise positions of the upper and lower boundaries, and the boundary condition imposed there, are irrelevant because the regions further from the shear layer plug up (a first illustration of Oldroyd's cloaking effect). We use the free characteristic lengthscale $\mathcal{L}$ to set $L_x = 1$, and impose $w_x(1, y) = 0$ and $w_y(x, \pm L_y) = 0$.

Numerical solutions for $Bi = 10$ and 100 are shown in Fig. 4, which plots the shear rate $\dot{\gamma}$ as a density over the (x, y)−plane with superposed contours of constant $w(x, y)$. The shear-layer structure illustrated by these numerical solutions is reproduced by Oldroyd's boundary-layer solution (Section 2.3.2), as also displayed in the figure.

For lower yield stress, we first note the Newtonian solution for $y > 0$,

$$w(x, y) = 1 - \sum_{n=1}^{\infty} \frac{\sin[(n - \frac{1}{2})\pi x]}{\pi(2n - 1)} e^{-(n - \frac{1}{2})\pi y}; \tag{52}$$

the solution in $y < 0$ can be obtained by symmetry, $w(x, y)$ being an odd function of y. For large y, we neglect all but the first term of the sum to find $w - 1 \sim -e^{-\frac{\pi}{2}y} \sin \frac{\pi}{2} x$; this can be matched with the far-field hodograph solution with $m = 1$ quoted in (47) by taking $A = -\frac{2}{\pi} Bi$, $X = 1$ and $Y = (2/\pi) \log(2Bi^{-1})$, ignoring the unit wall

Fig. 5. Numerical and asymptotic solutions for sliding half-planes (only showing the upper half-plane) with (a) $Bi = 1$, (b) $Bi = 0.25$ and (c) $Bi = 0.1$. The figure shows $\log_{10} \dot{\gamma}$ and equally spaced speed contours (blue), together with the hodograph prediction of the yield surface (dotted green) from (49).

speed, which can be added as an additional hodograph solution owing to the linearity of (31). The yield surface in (49) with these values must therefore characterize the remote plug when $Bi \ll 1$, as illustrated in Fig. 5, which shows numerical solutions for low Bi that converge to the asymptotic result as Bi is reduced.

Moving on to a sliding panel of unit half-width (taking the dimensional width to be $2\mathcal{L}$), we impose the boundary condition,

$$w(0, y) = \begin{cases} 0, & y < -1, \\ 1, & -1 < y < 1, \\ 0, & y > 1. \end{cases} \tag{53}$$

Again we consider a finite domain in which the length along the wall L_y is irrelevant if sufficiently wide, and the perpendicular length L_x is a parameter. Numerical solutions to this problem are shown in Fig. 6. When L_x is relatively small, the sliding panel drives a plug flow along the wall that is attached to the panel. The two free shear layers at the edges of the plug are identical to that for a certain sliding half-plane solution, owing to the isolation by the moving plug, and their structure
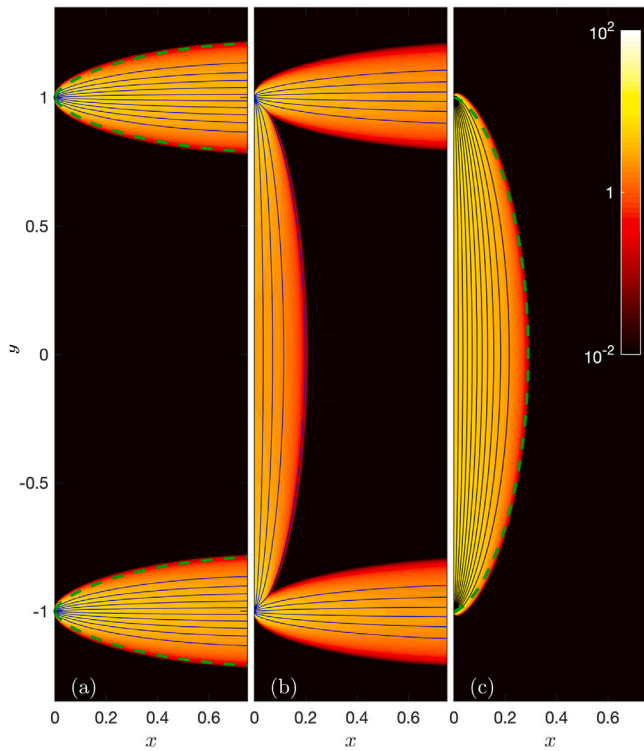
Fig. 6. Numerical solutions for sliding panels in domains of length (a) $L_x = 0.9$, (b) $L_x = 1$ and (c) $L_x = 1.1$, with $Ly = 2.5$ and Bi $= 100$ (not all the domain is plotted). Shown are density plots of $\log_{10} \dot{\gamma}$ and contours of constant w, together with the asymptotic predictions of Section 2.3.2 for the boundary-layer width in (a) and (c).

Fig. 7. Numerical solutions for a sliding panel with $L_x = L_y = 9$ and (a) Bi $= 0.5$ and (b) Bi $= 0.1$, showing a density plot of $\log_{10} \dot{\gamma}$ and contours of constant w together with the low-Bi hodograph predictions of the yield surface (dotted green) with $m = \frac{1}{2}$.

Fig. 8. Solutions for Bi $\gg 1$ in flow down an elliptical conduit. The inner cylinder has a speed and semi-major axis of unity and a semi-minor axis of 0.2; the outer cylinder has a semi-major (semi-minor) axis of 2 ($\frac{7}{4}$). Shown are (a) the yielded region expected from the wall-layer solution of Section 2.3.1 and (b) a numerical solution with Bi $= 500$ and $n = 1$. In (b), the (blue) lines are contours of constant speed and the shading shows $\log_{10} \dot{\gamma}$ over the yielded regions around the inner ellipse. The green dashed line show the Bi$^{-\frac{1}{2}}$ boundary-layer theory of (55).

is described by Oldroyd's boundary layer theory. With a larger domain length L_x, the plug breaks free and travels at a slower speed than the panel, creating a wall layer that also buffers the plug. In still longer domains, the plug connects to the stagnant zones attached to the wall on either side of the panel, eliminating the free shear layers and leaving only the wall layer. That wall layer is again described by Oldroyd's theory, as it must since the condition in (20) for a Bi$^{-\frac{1}{2}}$ layer is not valid.

To establish when the moving plug breaks free of the sliding panel, we revert to Oldroyd's minimum dissipation argument: when the plug is attached to the moving panel, the dissipation rate occurring over the two free shear layers converges to $2L_x$Bi for Bi $\to \infty$. Conversely, when the bulk of the fluid is stationary and there is only a wall layer, the dissipation rate has the limit, 2Bi. Thus, one expects the former configuration to be preferred when $L_x < 1$, and the latter for $L_x > 1$. With $L_x = 1$, and there is a moving plug with speed w_p bordered by both free shear layers and a wall layer, the dissipation rate amounts to 2Bi, given that the velocity jumps by $1 - w_p$ over the wall layer and by w_p over the free shear layers; any plug speed w_p then appears admissible. The configuration is also permitted by the modified force balance on the moving plug in (11) because $\ell_- = \ell_+ = 2$. Numerically, we find that the plug speed depends on the value of Bi.

We illustrate a solution with much lower Bi in Fig. 7. When $L_x \gg 1$, the corresponding Newtonian solution is

$$w = \frac{1}{\pi} \left(\tan^{-1} \frac{1-y}{x} + \tan^{-1} \frac{1+y}{x} \right) \sim \frac{2x}{\pi(x^2+y^2)} \tag{54}$$

for $x \gg 1$ and $y = O(x)$. Hence, the yield surface in (36) is relevant provided we take $m = \frac{1}{2}$ and $A = \sqrt{2\text{Bi}/\pi}$, which indicates that the plug lies at a distance of $O(\text{Bi}^{-\frac{1}{2}})$ from the panel. Again, the numerical solution agrees with this prediction. For smaller domain lengths L_x, the Newtonian solution in (54) must be replaced by another Fourier series
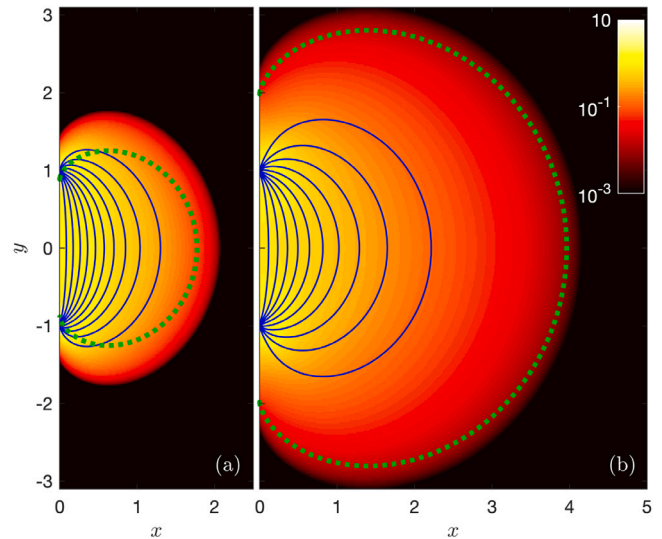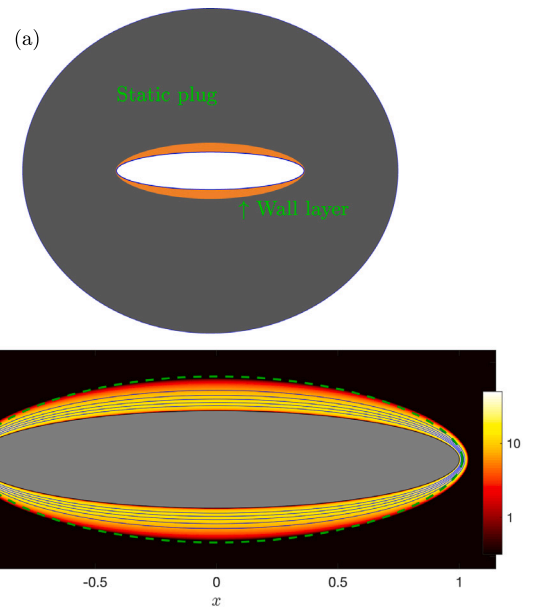
like that in (52), and the hodograph solution in Section 2.4.3 with $m = 1$ would then be relevant, rather than (36).

3.2. Oldroyd's knife

For uni-directional flow, Oldroyd's knife problem amounts simply to a change in the direction of motion: instead of the 2D flow driven by the knife moving parallel to its width, we consider the unidirectional motion arising when the knife is pulled along its (infinite) length (a third possibility, two-dimensional viscoplastic flow due to the transverse motion of the knife is considered by [58,59], and the flow around
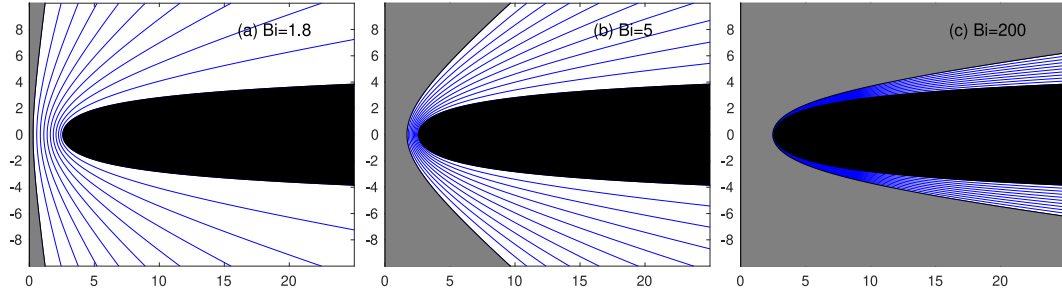
Fig. 9. Oldroyd's solution for flow of a Bingham fluid driven by a catenary moving past a plane wall for the three values of Bi indicated. Shown are contours of constant w, with the plug shaded grey and the catenary in black.

inclined plates is studied by [60,61]). Taking the knife to have speed V and width $2L$, we now impose the boundary conditions: $w(x,0) = 1$ for $|x| < 1$ and $w_y(x,0) = 0$ for $|x| > 1$. The latter condition ensures that the problem is slightly different from the sliding panel in Section 3.1 (other than a rotation of 90°).

Oldroyd's cartoon in Fig. 2 suggests that a wall layer should form around the knife at high Bingham number. However, one wonders whether the sharp ends of the knife are problematic and drive other flow as in the 2D problem [11]. Indeed, applying the wall theory of Section 2.3.1 is problematic as there is no pressure gradient and curvature. Thus, if there is a boundary layer, it cannot have the $Bi^{-\frac{1}{2}}$ scaling as in the 2D problem, but must follow Oldroyd's scaling.

To explore this situation further, we refer back to some of Oldroyd's other solutions for conduit flow. First, for flow between confocal ellipses driven by motion of one of the ellipses (as opposed to a pressure gradient) Oldroyd [3,4] points out that the flow must become localized to the inner wall at higher yield stresses, independent of the outer ellipse (Section 1.3), anticipating a boundary-layer-like structure to the flow. Indeed, as the aspect ratio of the inner ellipse becomes extreme, one envisions that the problem should converge to the conduit analogue of Oldroyd's knife; see Fig. 8(a). Awkwardly, however, the inner boundary has finite curvature, and so the boundary-layer analysis of Section 2.3.1 predicts that

$$w = \left(1 - \frac{\eta}{Y}\right)^{1+\frac{1}{n}}, \qquad 0 \le \eta \le Y = \left[\frac{(n+1)^n}{n^n \kappa}\right]^{\frac{1}{n+1}}, \tag{55}$$

where η is directed along the outward normal to the inner wall, which has local curvature κ. Here, we have taken the inner ellipse to have speed V and the outer ellipse to be stationary, and used the semi-major axis of the inner wall for L, so that $w_b = 1$ and $Y = w_p = 0$. Evidently, the boundary layer is thinnest at the ends where the curvature is highest; the layer becomes broad where curvature declines.

The boundary-layer structure in Fig. 8(a) can be confirmed by numerical computations, as shown in Fig. 8(b). We can provide further confirmation by reference to Oldroyd's solution for Bingham fluid between a moving catenary (with boundary $x = \frac{1}{2}\pi + \cosh y$, after a suitable choice of L) and a plane wall at $x = 0$. This solution makes use of special curvilinear coordinates (α, β) such that

$$(x, y) = (\alpha + \sin\alpha\cosh\beta, \beta + \cos\alpha\sinh\beta) \tag{56}$$

with $-\infty < \beta < \infty$ and $\alpha < \frac{1}{2}\pi$. For Bi less than about 1.7519, the fluid yields everywhere. For larger Bi, a plug appears against the plane wall, and the associated cloaking effect renders that boundary irrelevant and the problem similar to that of the flow around the tip of a knife. For the latter situation, the yield section is given by $\alpha_0 < \alpha < \frac{1}{2}\pi$, where

$$Bi = \left[\left(\frac{1}{2}\pi - \alpha_0\right)\cos\alpha_0 - 1 + \sin\alpha_0\right]^{-1}, \tag{57}$$

and the velocity field is given by

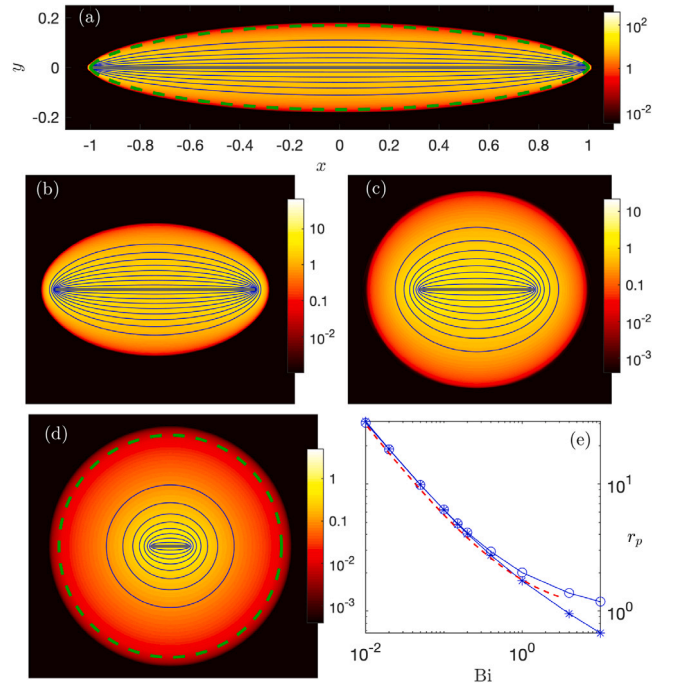$$w = Bi\left[(\alpha - \alpha_0)\cos\alpha_0 - \sin\alpha + \sin\alpha_0\right] \tag{58}$$

as shown in Fig. 9.

Fig. 10. Solutions for flow of a Bingham fluid ($n = 1$) past a knife along $-1 \le x \le 1$ and $y = 0$ at (a) Bi = 500, (b) Bi = 10, (c) Bi = 1 and (d) Bi = 0.1, showing contours of constant speed (blue lines) superposed on a density plot of $\log_{10}\dot{\gamma}$. The dashed line in (a) indicates the asymptotic solution for Bi ≫ 1 from Section 2.3.2. (e) The prediction $Bi\, r_p \log r_p = 1$ for the yield surface $r = r_p$ for Bi ≪ 1 (red dashed line), compared with numerical data of the vertical (stars) and horizontal (circles) distance from the origin to the yield surface. The dashed line in (d) also indicates this predicted yield surface.

For Bi ≫ 1, the flow becomes restricted to a boundary layer against the catenary. Indeed, the solution for Bi = 200 gives a convenient illustration of Oldroyd's expected knife flow. In this limit, the analytical solution reduces to

$$w = \left(1 - \frac{\eta}{Y}\right)^2, \qquad 0 \le \eta \le Y = \sqrt{2}\cosh\beta \tag{59}$$

and

$$(x, y) = \left(\frac{1}{2}\pi + \cosh\beta, \beta\right) + \epsilon\eta\frac{(-1, \sinh\beta)}{\cosh\beta}, \tag{60}$$

where β parameterizes a position along the catenary, η is the stretched normal coordinate, and $\epsilon = Bi^{-\frac{1}{2}}$. This solution recovers that of the boundary-layer theory in Section 2.3.1, given that the curvature of the catenary is $\kappa = \text{sech}^2\beta$ (cf. (55) with $n = 1$).

At this stage, it is also clear how the wall-layer theory of Section 2.3.1 break down for the knife: if we consider the catenary as a local approximation of the tip of the knife, then the local boundary-layer structure is now known. However, the solution also indicates

that the boundary layer continues to broaden further from the tip. Simultaneously, one expects (55) to fail when the curvature becomes sufficiently small to break the asymptotic scalings that led to it (Section 2.3.1). For the region away from the knife tips, we may instead turn to Oldroyd's boundary layer theory in Section 2.3.2 and the self-similar solution (25)–(26). In particular, we take $\varsigma \equiv x$, $\eta \equiv \epsilon^{-1}y$, $W_+ = 0$, $W_- = 2$ and $\sigma = -1$, and apply the boundary conditions $Y(\pm 1) = Y'(0) = 0$ on the first equation in (27). This gives the solution above the plate shown in Fig. 10(a) (with the solution below the plate given by symmetry), where it is compared with a numerical solution.

At lower Bi, the flow around the knife adopts the form illustrated in Fig. 10(b–d). For Bi $\ll 1$, the flow contours converge to circles at large distances from the knife, leading to a remote axisymmetric yield surface. The limiting solution near the plug therefore corresponds to the $m = 0$ hodograph solution, unlike that for the sliding panel (Fig. 7) which converges to the $m = 1$ dipole. Thus, even though the two boundary-layer solutions are the same (Figs. 6(c) and 10(a)), the different conditions along the wall or symmetry line ensure that the solution for lower yield stress are rather different.

In more detail, we observe that the Newtonian solution for the knife is, in fact,

$$w(x, y) = 1 - a\log r, \tag{61}$$

with $a = (\log R)^{-1}$ if $R \gg 1$ denotes the radius of a distant outer circular wall where $w = 0$ (cf. [4]). This dependence on the wall position (and the logarithmic form of (61)) arises due to the Stokes paradox for two-dimensional viscous flow. With weakly viscoplastic fluid, however, the yield stress becomes key further from the knife, arresting the flow and removing that paradox (cf. [62]). Thus, we cannot impose the outer boundary condition on (61), leaving a to be found from the match with the $m = 0$ hodograph solution in Section 2.4.1. In particular, we find $a = A = \mathrm{Bi}\, r_p$ and $1 = \mathrm{Bi}\, r_p \log r_p$, as also shown in Fig. 10(d,e).

4. Pressure-driven flows down ducts

The insights provided by the previous examples suggest how one can construct the flow pattern in the plastic limit for a duct of arbitrary shape. First, that pattern must consist of a patchwork of plugs, wall layers and free shear layers that form circular arcs with a fixed curvature given by Y/Bi. Because the thickness of the free shear layers always changes along their length, they must begin at a wall layer, widen up to a point of symmetry, and then thin back down to end at another wall layer. At the termini, the shear layer must meet the wall layers tangentially, as otherwise unmatched velocity gradients would arise at the junction between the two boundary layers. The curvature of the free shear layers is also connected to the shape of any embedded plugs: $\kappa = Y/\mathrm{Bi} = \ell/A$, where ℓ and A are the length of the perimeter and area of the plug. Further constraints arise from the cloaking effect: when a plug fully separates one boundary from the other, the local flow geometry must become independent of the veiled boundary and conform only to the shape of the adjacent one. Finally, the flow pattern that is achieved must minimize the dissipation rate in (12). But in the plastic limit, where all the dissipation takes place within the boundary layers and is due to the yield stress the net dissipation rate is given by $\iint_\Omega \tau \dot\gamma\, dx dy \sim \mathrm{Bi}\,\ell_B$, where ℓ_B is the total length of all the boundary layers. Thus, the realized flow pattern is that for which the boundary layers have shortest combined length, once all the other constraints are satisfied. Armed with these observations, we now consider some specific duct geometries that have proved popular in the past. The main notational difference from Section 2 is that the plastic limit corresponds to $w \ll 1$, rather than Bi $\gg 1$. Instead, Bi remains $O(1)$ and the pressure gradient Y must exceed a Bi–dependent threshold to initiate motion. Alternatively, if we exploit the prescribed pressure gradient to scale such that $Y = 1$, the plastic limit corresponds to Bi $\to \mathrm{Bi}_c$ for some critical Bingham number Bi_c.

4.1. Convex polygonal ducts

For a duct with walls that form a convex polygon of N sides, the preceding observations imply that the flow pattern will not consist of a single wall layer bordering a moving plug that occupies most of the conduit: the length of that wall layer will inevitably exceed the combined length of the boundary layers in a pattern in which free shear layers peel away from the wall to isolated stagnant zones in the vicinity of the vertices of the polygon. As long as these shear layers have the correct curvature, the flow must therefore adopt the corresponding flow pattern.

In more detail, if we assume that each circular arc can be made to isolate only a single vertex, then the moving plug is bordered by wall layers along the straight faces of the polygon and circular free shear layers with curvature κ that cut off the corners. Let ℓ_D and A_D denote the length of the perimeter and area of the duct, and θ_j denote the angle subtended by the jth vertex (in which case the arc of the corresponding plug has angle $\pi - \theta_j$). Then,

$$A = A_D - \kappa^{-2}(\alpha_N - \pi) \tag{62}$$

and

$$\ell = \ell_D - 2\kappa^{-1}(\alpha_N - \pi), \tag{63}$$

where

$$\alpha_N = \sum_{j=1}^{N} \cot\frac{1}{2}\theta_j \tag{64}$$

(the sum of the polygon's angles is $\sum_j \theta_j = (N-2)\pi$). The force balance on the plug now demands

$$\kappa = \frac{2(\alpha_N - \pi)}{\ell_D - \sqrt{\ell_D^2 - 2A_D(\alpha_N - \pi)}} \qquad \& \qquad Y = \kappa\mathrm{Bi}. \tag{65}$$

For a square duct, with sides of dimensional length L (dimensionless unit length), we insert four free shear layers along quarter circles of radius κ^{-1} that block off the corners, to find

$$\kappa = 2 + \sqrt{\pi} \qquad \& \qquad Y = (2 + \sqrt{\pi})\mathrm{Bi} \tag{66}$$

This result was stated previously in [24,29], although it was arrived at by a different, variational argument which states the correct choice for κ^{-1} is obtained as that which maximizes A/ℓ.

The correspondence of the variational argument with our asymptotic construction can be established by noting that the maximum value of A/ℓ arises for

$$\frac{dA}{d\kappa} = \frac{A}{\ell}\frac{d\ell}{d\kappa}. \tag{67}$$

But, because the circular arc of the free shear layer meets the straight wall layer tangentially, $dA = \kappa^{-1}d\ell$. Hence, $\kappa = \ell/A$, as in the asymptotic construction.

Viscoplastic flow down a square duct was advanced as a computational benchmark by Saramito & Rocquet [26]. In Fig. 11, we report more numerical solutions for Bingham fluid with $n = 1$, showing the convergence to the solution predicted above. Here, with the dimensionless pressure gradient Y scaled to unity, the critical yield stress at which flow commences is $\mathrm{Bi}_c = (2 + \sqrt{\pi})^{-1} \approx 0.2651$. The example with the largest yield stress (Bi = 0.26) is close to this threshold, and displays the free shear layer cutting off the corner and the much thinner wall layers.

More quantitative details of the convergence to the plastic limit are shown in Fig. 11(b), which plots the width of the boundary layer along the wall ϵ and central plug speed w_p against $\mathrm{Bi}_c - \mathrm{Bi}$. In particular, we observe the scalings $\epsilon = O(\mathrm{Bi}_c - \mathrm{Bi})$ and $w_p = O(\mathrm{Bi}_c - \mathrm{Bi})^2$. The arguments above that determine the critical Bingham number do not establish these details. Moreover, the boundary-layer theory of
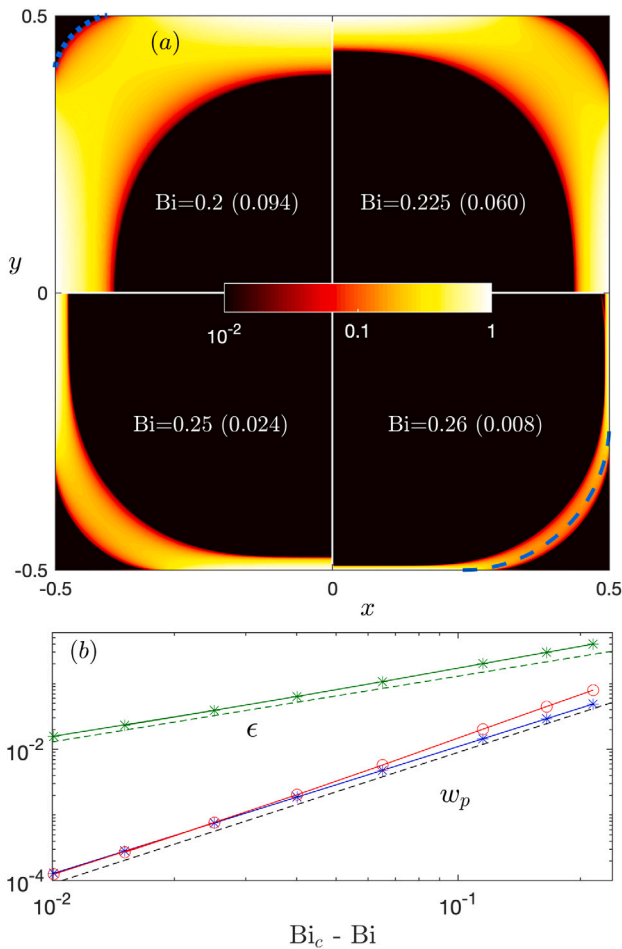
Fig. 11. (a) Numerical solutions for flow down a square conduit, showing a different solution in each quadrant corresponding to the Bingham number indicated. The density maps show the logarithm of the strain rate scaled by its maximum value in each case (with that value quoted in parentheses). The dotted line (upper left quadrant) shows the hodograph prediction with $m = 2$ and the dashed line (lower right quadrant) shows the asymptotic prediction for the location of the free shear layer when $\text{Bi} \to \text{Bi}_c$. (b) Numerical results for the thickness of the boundary layer against the wall ϵ and the speed w_p of the central plug against $\text{Bi} \to \text{Bi}_c = 1/(2+\sqrt{\pi})$ (stars). The red circles show the prediction $w_p = \frac{1}{2}\epsilon^2$, The dashed lines shows linear and quadratic scalings.

Section 2.3.1 indicates only that $w_p \sim \frac{1}{2}\epsilon^2$ for a Bingham fluid[1]. We must therefore advance beyond both analyses to establish the scalings. In particular, we may examine the force balance on the plug in (9). For $\text{Bi} < \text{Bi}_c$, the area and perimeter of the plug are both reduced by the boundary layers. But over the free shear layers, the radius of curvature is precisely $\text{Bi}/Y \approx \text{Bi}_c$, and so the change of area exactly matches the change in the length of the circular borders of the plug to leading order. The wall layers, however, contribute an area change of $O(\epsilon)$, correcting the Bingham number by a corresponding amount. Thus, $\text{Bi}_c - \text{Bi} = O(\epsilon)$, and we arrive at the observed scalings.

Fig. 11 also shows an example with lower Bi. In this case, the flow features a circular central plug and four small yield surfaces in each corner. These correspond to the hodograph solutions of Section 2.4 with $m = 0$ and $m = 2$. The shape of the latter matches well with the numerical solution, as indicated in the figure (and even though

---

[1] To adapt the results of Section 2.3.1 for $\text{Bi} \gg 1$ to the current situation, with $\text{Bi} \to \text{Bi}_c = O(1)$, we take $w = \epsilon^{1+\frac{1}{n}}\hat{w}$ and $Y = 1$, or $Y_{n+1} = \epsilon^{n+1}$, where ϵ is the boundary thickness. Then (17)–(19) still hold (with $\kappa = w_b = 0$), but for $\hat{w}$, and with $Y = 1$.

the lowest value of Bi presented is not that small), where we have employed the intersection of the yield surface with the wall to estimate the constant A (thereby avoiding the need for an explicit match, which is obscured by our neglect of the pressure gradient in Section 2.4).

4.2. Eccentric annulus

A second, even more popular geometry to use as a numerical benchmark is the flow through an eccentric annulus (*e.g.* [25,27,30,63,64]), as sketched in Fig. 12. If the outer radius is scaled to unity, then we have the parameters R and Δ describing the radius and sideways shift of the inner circular boundary. The configuration has important applications to oil extraction [65], and is also amenable to an insightful asymptotic analysis based on Reynolds lubrication theory in the limit of a thin gap [9] (see Appendix).

For the eccentric annulus, Szabo & Hassager [25,30] mapped out three possible flow patterns, illustrated in Fig. 13 for some of our own numerical solutions and characterized by

(i) a moving plug extending around the annulus (figure (13a, lower),

(ii) two moving plugs centred at the widest and narrowest sections (figure (13a,b), upper), or

(iii) a plug moving down the widest part and a static plug blocking the narrow part of the conduit figure (13b, lower).

Only the first and the last of these patterns consist purely of plugs and boundary layers in the plastic limit, and therefore are the only options at the onset of flow; see Fig. 12(a,b),

For the pattern shown in Fig. 12(a), there are two wall layers around each boundary and we have

$$\ell = 2\pi(1 + R) \qquad \& \qquad A = \pi(1 - R^2), \tag{68}$$

giving

$$Y = \frac{2\text{Bi}}{1 - R} \tag{69}$$

and a dissipation rate of $2\pi(1 + R)\text{Bi}$. As pointed out by Szabo & Hassager, this flow pattern persists well away from the plastic limit, with the sheared regions merely growing in size. The pattern is admissible because the plug isolates the two circular walls, demanding that the yielded zones adopt the circular symmetry of the two walls, in a further example of Oldroyd's cloaking principle.

The pattern in Fig. 12(b) is more complicated, but the geometry can be parameterized in terms of the angle θ_p at which the shear layer reaches the outer wall layer. The radius of curvature of the free shear layer and the plug perimeter length ℓ and area A can then be calculated. Applying the force balance on the moving plug then selects a particular value for θ_p for each pair (Δ, R). Simultaneously, we establish the scaled pressure gradient Y/Bi. The results are shown in Fig. 12(c,d), which plots Δ and θ_p against Y/Bi for four values of R, in the manner of Szabo & Hassager. Note that Szabo & Hassager approximate the free shear layer as a straight line, rather than a circular arc meeting the walls layers tangentially, although their predictions are very similar to those shown in Fig. 12 (see the dashed lines in Fig. 12c).

The two possible configurations in Fig. 12(a,b) lead to competing values for $Y = \kappa \text{Bi}$ for the same pairs of (Δ, R), as shown in Fig. 12(c). Assuming that the state with lower pressure gradient (larger Bi/Y) is the one that becomes realized first, we emerge with the selection indicated. Note that the angular position of the shear layer does not smoothly increase from $\theta_p = 0$, when the configuration in Fig. 12(b) first becomes selected on raising the sideways shift Δ of the inner cylinder. That is, when the annular moving plug breaks for $\Delta \approx \Delta_b(R)$, it does so to leave a blocked section of the conduit with finite angular extent. The critical sideways shift $\Delta \approx \Delta_b(R)$ is plotted in the inset to Fig. 12(b).

For $R \to 1$, the construction of the solution in Fig. 12(b) becomes more explicit: the angle θ_p satisfies

$$4Y(\pi - \theta_p + \tan\theta_p)[\frac{1}{2}Y(1 - R) - \text{Bi}] \sim \pi\text{Bi}^2, \tag{70}$$
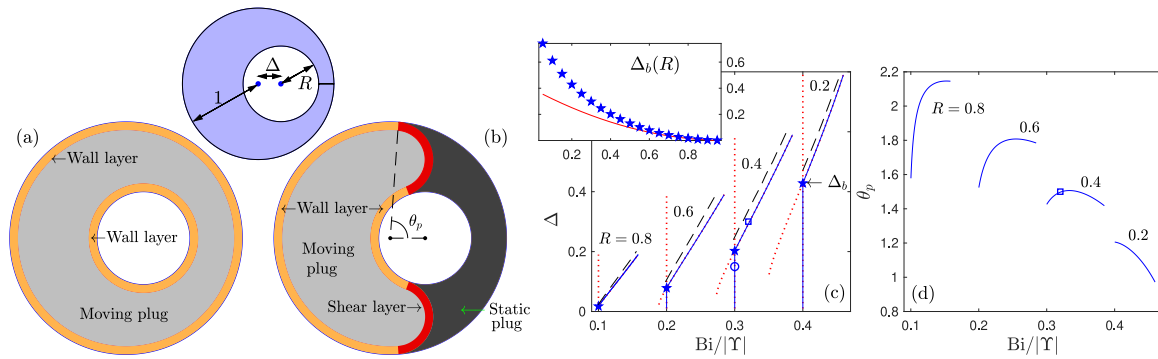
Fig. 12. Configuration for flow down an eccentric annulus in the plastic limit, showing the geometrical parameters in an inset at the top. Panels (a) and (b) show the two possible flow patterns at the initiation of flow suggested by Szabo & Hassager. The offset Δ and angular position of the shear layer θ_p (where it meets the outer wall layer) are plotted against the inverse pressure gradient Bi/Υ in (c,d). The circle and square indicate the configurations shown in (a,b); the dashed lines in (c) show results taken from Szabo & Hassager. The inset in (c) shows the critical sideways shift $\Delta_b(R)$ for which the annular plug breaks (stars), and the limit $\Delta \sim \frac{1}{8}\pi(1 - R)^2$ (solid line).
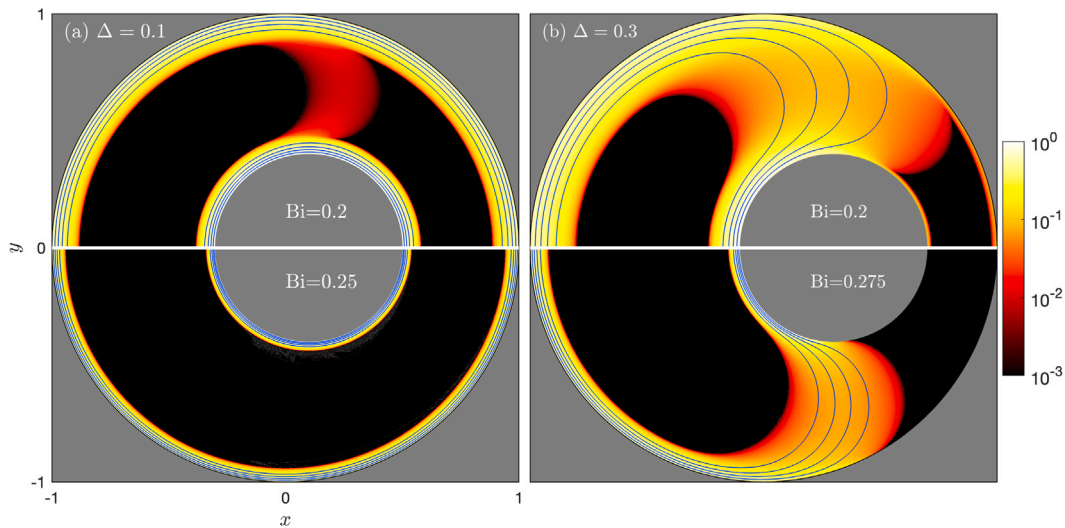

Fig. 13. Numerical solutions for viscoplastic flow down eccentric annuli with $R = 0.4$ and (a) $\Delta = 0.1$ and (b) $\Delta = 0.3$. Each panels shows solutions with the two values of Bi indicated. The blue lines show contours of constant w superposed on density maps of $\log_{10}\dot{\gamma}$.

with

$$\Delta = \frac{\Upsilon(1 - R) - 2\text{Bi}}{\Upsilon \cos\theta_p}.$$ (71)

The plug of the solution in Fig. 12(a) therefore breaks when

$$\frac{\text{Bi}}{\Upsilon} = \frac{1}{2}(1 - R), \quad \Delta = \frac{1}{8}\pi(1 - R)^2 \quad \& \quad \theta_p \rightarrow \frac{1}{2}\pi,$$ (72)

5. Conclusion

In this paper, we have enjoyed reviewing a series of papers by Oldroyd on viscoplastic flow. We also took the opportunity to mention some of the subsequent work motivated by Oldroyd (either knowingly or subliminally!) and establish some new results guided by his methods. In addition to formulating the now standard, three-dimensional formulation of the Bingham model [1], Oldroyd presented asymptotic analyses for nearly plastic boundary layers [2] and weakly viscoplastic conduit flows [3,4], together with exact solutions for certain conduit geometries [5–8]. These papers were based on the first half of Oldroyd's impressive Ph.D. Thesis at Trinity College, Cambridge. Commentary on the content of the second half of the thesis can be found elsewhere in this volume.

In retrospect, despite the immense impact of Oldroyd's work on viscoplasticity, Oldroyd was perhaps somewhat hamstrung by the unavailability of the computer at the time: his analytical methods are well complemented by numerical solution strategies, as we have exploited here. Had he been able to parallel, guide and extend his results with numerical computations, it is hard to see what could have limited his advances and how many decades of research may have been abbreviated.

Appendix. Lubrication theory for slender conduit

In this appendix we consider pressure-driven flow down a slender conduit with stationary walls, generalizing Walton & Bittleston's [9] analysis for an eccentric annulus to arbitrary shape. In such geometry, the flow adopts a distinctive pattern in which strongly sheared regions buffer a plug-like central flow from the walls; see the sample numerical solutions for narrow eccentric annuli in Fig. 14. The central region was
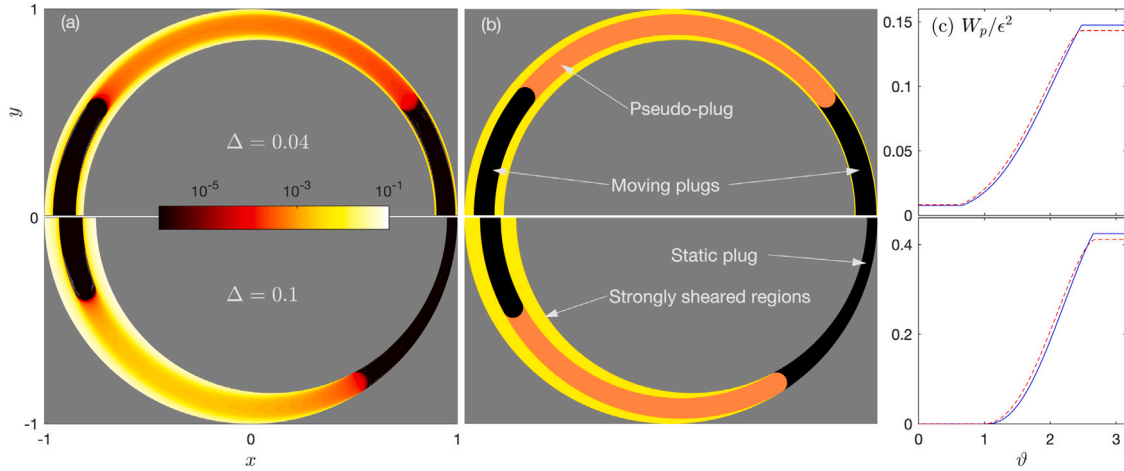
Fig. 14. Solutions for an eccentric annuli with $R = 0.85$, $\mathrm{Bi} = 0.05$, $Y = 1$ and the two values of Δ indicated (as drawn in the upper or lower halves of the panels). The numerical solutions (density maps of $\log_{10} \dot{\gamma}$) are shown in (a) and the flow configurations predicted by lubrication theory in (b). The speed along the centreline for both numerics (dashed) and asymptotics (solid) is shown in (c), scaled by ϵ^2 ($\epsilon = \frac{1}{2}(1 - R)$).

incorrectly identified as a true plug in some earlier papers, which it cannot be because the speed still varies along the centreline. This has led to an unfortunate and incorrect impression that the lubrication theory on which Walton & Bittleston's analysis is founded is inconsistent. Walton & Bittleston, however, simply observed that the asymptotic analysis had not been properly conducted for the central regions, and provided the correct construction of this "pseudo-plug".

Walton & Bittleston also pointed out that the moving plugs of patterns *(ii)* and *(iii)* from Section 4.2 (as illustrated in Fig. 13) persist in the thin-gap limit, becoming smaller features surrounding the midpoints of the gap at $\theta = 0$ and π (*cf.* Fig. 14). Here, we take the further opportunity to give a clearer and more general discussion of these types of plugs. Walton & Bittleston built such true plugs by encapsulating them within pseudo-plugs in a non-asymptotic fashion; instead, we provide an asymptotic construction that more closely matches numerical solutions.

We also consider the true plugs that can extend along the centreline of a narrow conduit, as illustrated by the plug of pattern *(i)* in Section 4.2 and Fig. 12(b)). In the geometry of a narrow conduit, such plugs can exist when the gap has almost uniform thickness, but must break when the walls become less parallel. This leads us to a thin-gap version of the condition derived at the end of Section 4.2.

A.1. Thin-gap formulation

To begin, we return to (13), written in the more basic form,

$$\frac{\partial}{\partial \eta}(h T_{\eta z}) + \epsilon \frac{\partial T_{\varsigma z}}{\partial \varsigma} = -h Y_{n+1}, \tag{A.1}$$

where

$$\begin{pmatrix} T_{\varsigma z} \\ T_{\eta z} \end{pmatrix} = \left(\dot{\Gamma}^{n-1} + \frac{\mathrm{Bi}_n}{\dot{\Gamma}} \right) \begin{pmatrix} \epsilon h^{-1} w_{\varsigma} \\ w_{\eta} \end{pmatrix} \tag{A.2}$$

if $\sqrt{T_{\eta z}^2 + T_{\varsigma z}^2} > \mathrm{Bi}_n$, and $w_{\eta} = w_{\varsigma} = 0$ otherwise. Here, we have also rescaled to prepare the path for a lubrication analysis by setting

$$(T_{\varsigma z}, T_{\eta z}) = \epsilon^n (\tau_{\varsigma z}, \tau_{\eta z}), \qquad \dot{\Gamma} = \epsilon \dot{\gamma} = \sqrt{w_{\eta}^2 + \epsilon^2 h^{-2} w_{\varsigma}^2} \tag{A.3}$$

$$Y = \epsilon^{-n-1} Y_{n+1} \quad \& \quad \mathrm{Bi} = \epsilon^{-n} \mathrm{Bi}_n. \tag{A.4}$$

We have $w = 0$ at the walls, $\eta = \pm \mathcal{Y}(\varsigma)$, once we select $\eta = 0$ to represent the centreline of the conduit.

To $O(\epsilon)$, (A.1) implies that

$$T_{\eta z} = -\eta Y_{n+1}, \tag{A.5}$$

given that the leading-order equations are symmetrical about $\eta = 0$. Note that one cannot avoid this leading-order solution by inserting a rigid plug in the middle of the channel over which the scaling of the stress components is different: $T_{\eta z}$ must remain $O(1)$ there in order to achieve continuity with the sheared regions across any yield surfaces, and breaking the main balance in (A.1) by promoting the other stress component implies that $T_{\varsigma z} = O(\epsilon^{-1})$, which violates the yield condition. Unavoidably, the flow must therefore break down into a central section of the conduit where $|T_{\eta z}| < \mathrm{Bi}_n$, bordered by two regions against the walls with $|T_{\eta z}| > \mathrm{Bi}_n$, focussing on the situation in which the shear stress at the walls does breach the yield stress; *i.e.* that $\mathcal{Y} Y_{n+1} > \mathrm{Bi}_n$. If the shear stress at the wall is any lower, the pressure gradient is insufficient to drive flow down that part of the conduit. In other words, the conduit becomes blocked (*i.e.* spanned by a stagnant rigid plug) when $Y \geq \mathcal{Y}$. Such a blocked region appears the lower of the solutions in Fig. 14.

A.2. Main sheared regions; $|T_{\eta z}| > \mathrm{Bi}_n$ ($\mathcal{Y} Y_{n+1} > \mathrm{Bi}_n$)

Over the regions against the walls (shown in yellow in Fig. 14(b)), the yield stress is clearly breached, and the constitutive law demands that

$$T_{\eta z} = |w_{\eta}|^{n-1} w_{\eta} + \mathrm{Bi}_n \mathrm{sgn}(w_{\eta}). \tag{A.6}$$

Thence, $\mathrm{sgn}(w_{\eta}) = -\mathrm{sgn}(\eta)$ and

$$w = W_p \left[1 - \left(\frac{|\eta| - Y}{\mathcal{Y} - Y} \right)^{1 + \frac{1}{n}} \right], \tag{A.7}$$

where $\eta = \pm Y$, with

$$Y = \frac{\mathrm{Bi}_n}{Y_{n+1}}, g \tag{A.8}$$

are the locations where $|T_{\eta z}|$ decreases to Bi_n and

$$w \to W_p \equiv \frac{n Y_{n+1}^{\frac{1}{n}}}{n+1} (\mathcal{Y} - Y)^{1 + \frac{1}{n}}. \tag{A.9}$$

At first sight, and in view of the apparent dominance of the stress component $T_{\eta z}$, the levels $\eta = \mathcal{Y}$ appear to be genuine yield surfaces with the central core, $|\eta| < Y$ (where $|T_{\eta z}| < \mathrm{Bi}_n$), being a rigid plug. However, the "plug" speed W_p depends on $\mathcal{Y}(\varsigma)$ and therefore cannot be constant, except when the conduit has constant width. This confusion suggests that there is an inconsistency in lubrication theory for viscoplastic fluids. However, this is not case: the true issue is that the constitutive law has been incorrectly dealt with in the analysis over the regions that w_{η} becomes small [9].

A.3. The pseudo-plug; $|T_{\eta z}| < \mathrm{Bi}_n$ ($\mathcal{Y}Y_{n+1} > \mathrm{Bi}_n$)

When $|\eta| \to Y$, the preceding analysis indicates that $w_\eta \to 0$. This implies that the approximation $\dot{\Gamma} \approx |w_\eta|$ is inconsistent in (A.2). If w_η becomes $O(\epsilon)$, and

$$w = W_p(\varsigma) + \epsilon w_1(\varsigma, \eta) + \cdots \tag{A.10}$$

the correct approximation is

$$\dot{\Gamma} \sim \epsilon \sqrt{W_{p\varsigma}^2 + w_{1\eta}^2}. \tag{A.11}$$

In turn, this implies that

$$\begin{pmatrix} T_{\varsigma z} \\ T_{\eta z} \end{pmatrix} \sim \frac{\mathrm{Bi}_n}{\dot{\Gamma}} \begin{pmatrix} W_{p\varsigma} \\ w_{1\eta} \end{pmatrix}. \tag{A.12}$$

In other words, $T_{\varsigma z}^2 + T_{\eta z}^2 \sim \mathrm{Bi}_n^2$, and so, in view of (A.5), we may complete a solution for the region $|\eta| < Y$ in which the stress is held at the yield stress to leading order. This is Walton & Bittleston's "pseudo-plug" (and shown in Fig. 14(b) by the orange region).

The correct lubrication solution therefore consists of relatively strongly sheared zones against the walls, where the velocity profile is (A.7), bordering a central pseudo-plug with $w \approx W_p$. Different asymptotic solutions apply over the two regions and a formal asymptotic solution demands that the two be matched across the "fake" yield surfaces $\eta = \pm Y$. As noted by Walton & Bittleston, this can be accomplished by finding a third solution over a narrow layer surrounding $\eta = \pm Y$ with a thickness of $O(\epsilon^{\frac{2}{3}})$ (see [66]). Thus, the analysis boils down to an exercise in matched asymptotic expansions. The finer details of this matching calculation are not, however, needed once we require that w and the stress remain continuous at $\eta = \pm Y$.

We further note that

$$w_{1\eta} = -\frac{\eta Y_{n+1} |W_{p\varsigma}|}{\sqrt{Y^2 - \eta^2}} \tag{A.13}$$

over the pseudo-plug (the divergence of $w_{1\eta}$ for $\eta \to \pm Y$ is demanded by the need to match with the more highly sheared regions beyond). The steps leading to (A.13) break down, however, if $W_{p\varsigma}$ is not $O(1)$. Indeed, Walton & Bittleston argue that a true plug must inevitably appear around the points of symmetry where $W_{p\varsigma} = 0$. This observation led them to refine the theory at the widest and narrowest sections of the eccentric annulus, and embed a true plug there (see Fig. 14). For the arbitrarily shaped conduit considered here, and given that $W_p(\varsigma)$ is dictated by $\mathcal{Y}(\varsigma)$, the symmetry points correspond to the maxima or minima in the thickness. The more general point, however, is that the pseudo-plug analysis requires revision where $W_{p\varsigma}$, or $\mathcal{Y}_\varsigma$, becomes small.

A.4. Embedded plugs

If the thickness of the conduit is nearly constant, we set $\mathcal{Y} = \mathcal{Y}_0 + \delta \mathcal{Y}_1(\varsigma)$, where the scale of the wall variation δ is small, but could be $O(\epsilon)$: $\epsilon < \delta \ll 1$. We then pursue a different asymptotic expansion that can permit the central core of the conduit to become truly plugged up. For the task, we focus on the sheared region against the wall at $\eta = +\mathcal{Y}$ and open the expansion with the sequences,

$$T_{\eta z} = -\eta Y_{n+1} + \delta T_1 + \cdots, \quad w = w_0 + \delta w_1 + \cdots, \tag{A.14}$$

Since $T_{\varsigma z}$ remains small over this region, equation (A.1) now furnishes at, $O(\delta)$,

$$T_{1\eta} + \frac{\epsilon}{\delta} \kappa \eta Y_{n+1} = 0, \tag{A.15}$$

and so

$$T_1 = T_* + \frac{\epsilon}{2\delta} \kappa Y_{n+1}(Y^2 - \eta^2) \tag{A.16}$$

for some integration "constant", $T_*(\varsigma)$.

To $O(\epsilon^2)$, the constitutive law remains (A.6), and so we again find the leading-order velocity profile in (A.7) and (A.9) for w_0, but now with the replacement $\mathcal{Y} \to \mathcal{Y}_0$. At $O(\delta)$,

$$T_1 = n[Y_{n+1}(|\eta| - Y)]^{1 - \frac{1}{n}} w_{1\eta}. \tag{A.17}$$

At the yield surface, $\eta = Y + \delta Y_1$, we must have

$$T_{\eta z} = -(Y + \delta Y_1)Y_{n+1} + \delta T_1(\varsigma, Y) + \cdots = -\mathrm{Bi}_n, \tag{A.18}$$

which implies an $O(\delta)$ shift in position given by

$$Y_1 = \frac{T_*}{Y_{n+1}}. \tag{A.19}$$

In view of the boundary condition on the wall,

$$0 = w_0(\varsigma, \mathcal{Y}_0) + \delta[w_1(\varsigma, \mathcal{Y}_0) + \mathcal{Y}_1 w_{0\eta}(\varsigma, \mathcal{Y}_0)] + \cdots, \tag{A.20}$$

we may further calculate $w_1(\varsigma, \eta)$. We record the result,

$$w_1(\varsigma, Y) = -(\mathcal{Y}_0 - Y)^{\frac{1}{n}} Y_{n+1}^{\frac{1}{n}} Y_{1*}, \tag{A.21}$$

where

$$Y_{1*} = Y_1 - \mathcal{Y}_1 - \frac{\epsilon}{\delta} \kappa (\mathcal{Y}_0 - Y) \frac{(n+1)\mathcal{Y}_0 + (2n+1)Y}{2(n+1)(2n+1)}. \tag{A.22}$$

For the central core to be a true plug, the corresponding speed,

$$w_p = w_0(\varsigma, Y) + \delta[w_1(\varsigma, Y) + Y_1 w_{0\eta}(\varsigma, Y)] + \cdots \tag{A.23}$$

$$= \frac{n Y_{n+1}^{\frac{1}{n}}}{n+1}(\mathcal{Y}_0 - Y)^{1 + \frac{1}{n}} + \delta w_1(\varsigma, Y) + \cdots, \tag{A.24}$$

must be constant; hence, Y_{1*} must also be constant.

A.4.1. Force balance

To $O(\epsilon^2, \epsilon\delta)$, the signed perimeter of the plug in (11) is

$$\ell_+ - \ell_- = 2S_p + 2\sigma\pi\epsilon Y. \tag{A.25}$$

if the plug has finite arc length $S_p = \varsigma_*^+ - \varsigma_p^-$ and ends at $\varsigma = \varsigma_*^\pm$ where it is rounded off by circular arcs of radius ϵY, following the guidelines established in the main text, and as illustrated by the (black) plugs in Fig. 14. We have also included a sign $\sigma = \pm 1$ to account for the fact that the fluid in $\varsigma > \varsigma^+$ and $\varsigma < \varsigma_-$ may be flowing slower or faster (respectively), but the yielded sections for $|\eta| > Y$ are always slower. The corresponding plug area is

$$A = 2\epsilon \left(Y S_p + \delta \int_{s_*^-}^{s_p^+} Y_1 \mathrm{d}\varsigma \right) + \pi\sigma\epsilon^2 Y^2, \tag{A.26}$$

if the plug is convex (concave) when the adjacent fluid is slower (faster); cf. the ends of two plugs in Fig. 14. Force balance ($YA = (\ell_+ - \ell_-)\mathrm{Bi}$) therefore recovers $Y_{n+1}Y = \mathrm{Bi}_n$ at leading order, and demands

$$\delta \int_{s_*^-}^{s_p^+} Y_1 \mathrm{d}\varsigma = \frac{1}{2}\sigma\epsilon\pi Y^2 \tag{A.27}$$

at $O(\epsilon, \delta)$.

For an uninterrupted plug that spans a conduit of arc length S, there is no need to include any circular end-caps or consider the choice of sign (the plug is always faster). Instead, the corresponding results are

$$\ell = 2S, \quad A = 2\epsilon \left(Y S + \delta \int_0^S Y_1 \mathrm{d}\varsigma \right), \quad \int_0^S Y_1 \mathrm{d}\varsigma = 0. \tag{A.28}$$

A.4.2. The lateral stress on the plug

Finally, we consider the lateral stress $T_{\varsigma z}$ that acts on the plug: over the sheared layer, the constitutive law in (A.2) demands that this stress component is $O(\epsilon\delta w_{1\varsigma})$. But no such constraint applies over the plug, where the stress state is indeterminate and must only satisfy the yield condition

$$T_{\varsigma z}^2 + T_{\eta z}^2 < \mathrm{Bi}_n^2, \quad \text{or} \quad T_{\varsigma z}^2 < Y_{n+1}^2(Y^2 - \eta^2), \tag{A.29}$$

in view of the leading-order form of $T_{\eta z}$ which does apply across the plug. Thus, $T_{\varsigma z}$ could be $O(1)$ here, although it must become small at the yield surfaces in order to remain continuous with the solution in $|\eta| > Y$. Given this, we integrate (A.1) over the plug, to find, at $O(\delta)$,

$$2T_1(\varsigma, Y) + \frac{\epsilon}{\delta} \frac{\partial}{\partial \varsigma} \int_{-Y}^{Y} T_{\varsigma z} \mathrm{d}\eta = 0. \tag{A.30}$$

In the problems we consider, there are positions along the conduit where symmetry demands that $T_{\varsigma z} = 0$. Necessarily, these positions correspond to extrema in the conduit half thickness $\mathcal{Y}$. Thus, denoting $\varsigma = \varsigma_0$ by one such position, (A.30) may be integrated to give

$$\frac{\epsilon}{\delta} \int_{-Y}^{Y} T_{\varsigma z} \mathrm{d}\eta = -2Y_{n+1} \int_{\varsigma_0}^{\varsigma} Y_1(\hat{\varsigma}) \mathrm{d}\hat{\varsigma}. \tag{A.31}$$

Although we do not know $T_{\varsigma z}$ within the plug, we do know this stress component if the plug terminates at $\varsigma = \varsigma_p^+$, as there it must given by the pseudo-plug solution,

$$T_{\varsigma z} = Y_{n+1} \sqrt{Y^2 - \eta^2} \, \mathrm{sgn}(W_{p\varsigma}). \tag{A.32}$$

At this position, we may therefore evaluate the integral on the left of (A.31) to find

$$\sigma \frac{\epsilon \pi}{4\delta} Y^2 = \int_{\varsigma_0}^{\varsigma_p^+} Y_1(\varsigma) \mathrm{d}\varsigma, \tag{A.33}$$

since $\mathrm{sgn}(W_{p\varsigma}) \equiv -\sigma$ at the edge of the plug. This condition is in agreement with (A.27), reinforcing the notion that an isolated plug must be terminated by certain circular arcs. Nevertheless, (A.33) provides a further constraint on a plug that spans the conduit, since if the net lateral stress on the right reaches the limit given by the left-hand side anywhere along the conduit, the plug must break at that position.

A.4.3. Walton & Bittleston's embedded plugs

When there is a localized plug embedded around a point of symmetry, we follow Walton & Bittleston and argue that the span of that structure is relatively small, but not as narrow as the conduit. An expansion of the conduit half-thickness about its extremum gives

$$\mathcal{Y} \sim \mathcal{Y}_0 + \frac{1}{2} \mathcal{Y}''(0)(\varsigma - \varsigma_0)^2 + \cdots, \tag{A.34}$$

indicating that $\delta \mathcal{Y}_1 \equiv \frac{1}{2} \mathcal{Y}''(0)(\varsigma - \varsigma_0)^2$, or $\varsigma - \varsigma_0 = O(\delta^{\frac{1}{2}})$. To account for this narrower scale, we therefore set $\varsigma = \varsigma_0 + \delta^{\frac{1}{2}} \xi$, in which case (A.33) becomes

$$\frac{1}{4} \sigma \epsilon \pi Y^2 = \delta^{\frac{3}{2}} \int_0^{\xi_*} Y_1(\xi) \mathrm{d}\xi, \tag{A.35}$$

where the plug ends at $\varsigma = \varsigma_p^{\pm} = \varsigma_0 \pm \delta^{\frac{1}{2}} \xi_*$. Thus, $\delta = \epsilon^{\frac{2}{3}}$, implying that the arclength of the plug is $O(\epsilon^{\frac{1}{3}})$ as found by Walton & Bittleston. Note that we should take $\sigma = +1$ if the plug sits in the widest part of the conduit (and is convex), and $\sigma = -1$ if it occupies the narrowest part (the plug then being concave).

We may also neglect the terms of order $\epsilon \delta^{-1} = \epsilon^{\frac{1}{3}}$ in (A.22) to arrive at $Y_1 = Y_{1*} + \mathcal{Y}_1 = Y_{1*} + \frac{1}{2} \mathcal{Y}_0''(0) \xi^2$. We further fix Y_{1*} so that the true plug joins the pseudo-plug at $\xi = \xi_*$ without a jump in thickness and speed. For this task, we note $\eta = Y$ at the upper fake yield surface and

$$W_p = W_p(\varsigma_0) + \frac{1}{2} \delta Y_{n+1}^{\frac{1}{n}} (\mathcal{Y}_0 - Y)^{\frac{1}{n}} \mathcal{Y}_0'' \xi^2, \tag{A.36}$$

whereas the plug width and speed are given by $Y + \delta Y_1(\xi)$ and (A.21) and (A.24). Hence, $Y_1(\xi_*) = 0$, or $Y_{1*} = -\mathcal{Y}_1(\xi_*) = -\frac{1}{2} \mathcal{Y}_0''(0) \xi_*^2$, leading to

$$Y_1 = -\frac{1}{2} \mathcal{Y}_0''(0)(\xi_*^2 - \xi^2). \tag{A.37}$$

The condition (A.35) now implies

$$\frac{1}{4} \pi Y^2 = \frac{1}{3} |\mathcal{Y}_0''(0)| \xi_*^3, \tag{A.38}$$

since $\sigma \equiv -\mathrm{sgn}(\mathcal{Y}''(0))$. That is,

$$\xi_* = \left[\frac{3\pi Y^2}{4|\mathcal{Y}''(0)|} \right]^{\frac{1}{3}}. \tag{A.39}$$

Although we arrive at Walton & Bittleston's scale for the embedded plug here, the detailed derivation is different, leading to a slightly different prediction for the extent of the plug. In particular, we do not assume that the plug is nested within a pseudoplug. Indeed, the plug structure in their Fig. 4 is not seen in the numerical solution of Fig. 14, where the embedded plugs directly adjoin the main sheared regions and take a different, distinctive shape. We further account for the abrupt end of the plug at $\varsigma - \varsigma_0 = \delta^{\frac{1}{2}} \xi_*$ differently. There, we introduce circular end-caps with a finer scale in arc length, a construction that conforms to the guidelines established in the main text and the observed plug structure of the numerical solutions, whilst guaranteeing that the force balance calculation of Appendix A.4.1 matches the extensional stress condition in Appendix A.4.2.

A.4.4. Nearly uniform conduits

As pointed out in slightly different contexts by Frigaard & Ryan [67] and Liu et al. [68], one can also consider the genuine plugs that arise in flows that are nearly uniform along their centrelines. For such a scenario, we prescribe the perturbation to the wall and (A.33) then constrains when the central plug will break as the amplitude δ is increased. Denoting an average across the conduit by $\langle \ldots \rangle$, (A.28) demands $\langle Y_1 \rangle = 0$ up to the moment that breakage occurs. Hence, from (A.28),

$$Y_1 = \mathcal{Y}_1 - \langle \mathcal{Y}_1 \rangle. \tag{A.40}$$

As pointed out above, the plug remains intact unless the net stress component $\int_{-Y}^{Y} T_{\varsigma z} \mathrm{d}\eta$ reaches the limit in (A.33) somewhere along the channel. That is, unless

$$\sigma \frac{\epsilon \pi}{4\delta} Y^2 > \int_{\varsigma_0}^{\varsigma} \mathcal{Y}_1 \mathrm{d}\varsigma. \tag{A.41}$$

A.5. The eccentric annulus

For the eccentric annulus, the geometry is conveniently expressed in terms of the polar angle ϑ from the centre of the circular midline (which lies at $(x, y) = (\frac{1}{2}\Delta, 0)$): $\varsigma = \frac{1}{2}(1 + R)\vartheta \approx \vartheta$,

$$\begin{pmatrix} x - \frac{1}{2}\Delta \\ y \end{pmatrix} = [\frac{1}{2}(1 + R) - \epsilon\eta] \begin{pmatrix} \cos \vartheta \\ \sin \vartheta \end{pmatrix}, \tag{A.42}$$

$$\mathcal{Y}(\varsigma) = 1 - \chi \cos \vartheta, \quad \epsilon = \frac{1}{2}(1 - R), \quad \chi = \frac{\Delta}{1 - R}. \tag{A.43}$$

The predictions of the asymptotic analysis are well matched by the two narrow-gap numerical solutions shown in Fig. 14, which clearly illustrate the main sheared regions, pseudo-plugs and true plugs, even though the parameter $\epsilon = 0.075$ is not particularly small.

Walton & Bittleston's embedded, moving plugs are centred at the points of symmetry given by $(\eta, \vartheta) = (0, \pi)$ and (provided the narrow side is not plugged up) $(\eta, \vartheta) = (0, 0)$. At both locations,

$$\mathcal{Y}_0(0) \equiv 1 \mp \chi \quad \& \quad |\mathcal{Y}_0''(0)| \equiv \chi. \tag{A.44}$$

From (A.39), we therefore observe that these plugs span similar angular intervals of half-width,

$$\delta^{\frac{1}{2}} \xi_* = \left(\frac{3\pi \epsilon Y^2}{4\chi} \right)^{\frac{1}{3}}. \tag{A.45}$$

The corresponding result from Walton & Bittleston is (in the current notation),

$$\delta^{\frac{1}{2}} \xi_* = \left(\frac{3\epsilon Y^2}{\chi} \right)^{\frac{1}{3}}, \tag{A.46}$$

which differs by about 8%. On the other hand, if the narrow side of annulus is blocked up by a stagnant plug, flow only recommences
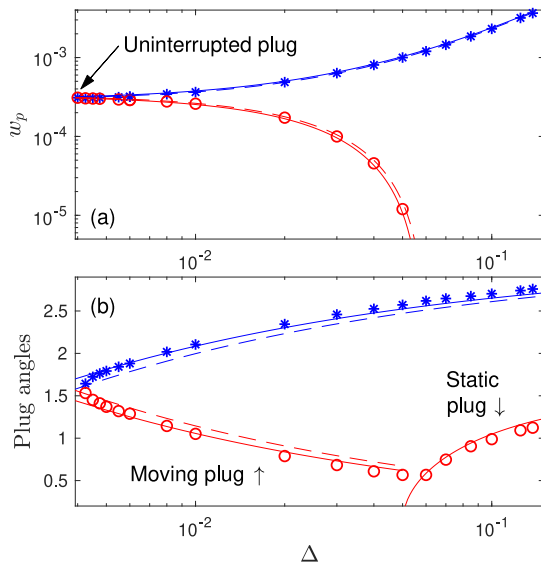
Fig. 15. Numerical data (stars and circles) and asymptotic predictions (solid lines) for (a) plug speeds and (b) plug angles (measured along the centreline for the numerical solution), with $Bi = 0.05$ and $R = 0.85$. Walton & Bittleston's predictions are shown by the dashed lines.

where $Y < \mathcal{Y}$, or $|\vartheta| > \cos^{-1}[(1 - Y)/\chi]$. The two examples in Fig. 14 straddle the division $\chi = 1 - Y$ at which the plug is predicted to break free of the walls. Numerical results for the speeds and angular borders of the plugs are collected together in Fig. 15 and compared with the prediction of asymptotic theory (and that of Walton & Bittleston). The asymptotic analysis applies strictly only when the moving plugs are small (justifying the introduction of (A.34)). However, as Δ becomes smaller, these plugs grow in size and eventually merge into the single plug that extends all around the annulus.

For the uninterrupted plug, we take $\chi \equiv \delta \ll 1$, $\mathcal{Y}_0 = 1$ and $\mathcal{Y}_1 \equiv -\cos\vartheta = Y_1$. The condition (A.41) then demands that the plug will break when

$$\delta = \frac{1}{4}\pi\epsilon Y^2 \qquad \text{or} \qquad \Delta = \frac{1}{8}\pi Y^2(1 - R)^2, \qquad (A.47)$$

at the positions, $\vartheta = \pm\frac{1}{2}\pi$. In the plastic limit, the sheared regions in $1 \geq |\eta| > Y$ shrink to $O(Bi^{-\frac{1}{2}})$ boundary layers for $Y \equiv Bi_n/Y_{n+1} \to 1$. This implies that the plug breaks for the conditions in (72), reproducing the results in Section 4.2. Note that, because the analysis for the localized moving plugs assumes that these features are relatively small, the criterion for their merger that one can extract from (A.45) is unlikely to coincide with (A.47). Indeed there is a disagreement, as can be seen in Fig. 15 where the Δ-axis ends on the left at the value given by (A.47), $\Delta \approx 3.9 \times 10^{-3}$, but here (A.45) still predicts separate plugs. Note that the numerical computations reported in this figure suggest that the uninterrupted plug breaks at a value closer to $\Delta = 4.2 \times 10^{-3}$, but this discrepancy is of the order of the small parameter $\epsilon = \frac{1}{2}(1 - R)$.

References

[1] J.G. Oldroyd, A rational formulation of the equations of plastic flow for a Bingham solid, Proc. Camb. Philos. Soc. 43 (1947) 100–105.
[2] J. Oldroyd, Two-dimensional plastic flow of a Bingham solid: a plastic boundary-layer theory for slow motion, Math. Proc. Camb. Phil. Soc. 43 (3) (1947) 383–395.
[3] J. Oldroyd, Rectilinear plastic flow of a Bingham solid: I. Flow between eccentric circular cylinders in relative motion, Math. Proc. Camb. Phil. Soc. 43 (3) (1947) 396–405.
[4] J.G. Oldroyd, Rectilinear plastic flow of a Bingham solid: II. Flow between confocal elliptic cylinders in relative motion, Math. Proc. Camb. Phil. Soc. 43 (4) (1947) 521–532.
[5] J.G. Oldroyd, Rectilinear plastic flow of a Bingham solid: III. A more general discussion of steady flow, Math. Proc. Camb. Phil. Soc. 44 (2) (1948) 200–213.
[6] J.G. Oldroyd, Rectilinear plastic flow of a Bingham solid: IV. Non-steady motion, Math. Proc. Camb. Phil. Soc. 44 (2) (1948) 214–228.
[7] J.G. Oldroyd, Rectilinear flow of non-Bingham plastic solids and non-Newtonian viscous liquids. I, Math. Proc. Camb. Phil. Soc. 45 (4) (1949) 595–611.
[8] J.G. Oldroyd, Rectilinear flow of non-Bingham plastic solids and non-Newtonian viscous liquids II, Proc. Camb. Phil. Soc. 47 (1951) 410–418.
[9] I.C. Walton, S.H. Bittleston, The axial flow of a bingham plastic in a narrow eccentric annulus, J. Fluid Mech. 222 (1991) 39–60.
[10] W. Prager, On slow visco-plastic flow, Stud. Math. Mech. (1954) 208–216.
[11] N. Balmforth, R.V. Craster, D.R. Hewitt, S. Hormozi, A. Maleki, Viscoplastic boundary layers, J. Fluid Mech. 813 (2017) 929–954.
[12] R. Hill, The Mathematical Theory of Plasticity, Oxford University Press, 1950.
[13] W. Prager, P.G. Hodge, Theory of Perfectly Plastic Solids, Wiley, 1951.
[14] K.v. Hohenemser, W. Prager, Über die ansätze der mechanik isotroper kontinua, ZAMM Z. Angew. Math. Mech. 12 (4) (1932) 216–226.
[15] W. Prager, Mécanique des solides isotropes au delà du domaine élastique, vol. 87, Gauthier-Villars Paris, 1937.
[16] D. Doraiswamy, A.N. Mujumdar, I. Tsao, A.N. Beris, S.C. Danforth, A.B. Metzner, The Cox–Merz rule extended: A rheological model for concentrated suspensions and other materials with a yield stress, J. Rheol. 35 (1991) 647–685.
[17] P. Saramito, A. Wachs, Progress in numerical simulation of yield stress fluid flows, Rheol. Acta 56 (2017) 211–230.
[18] J.-M. Piau, Viscoplastic boundary layer, J. Non-Newton. Fluid Mech. 102 (2002) 193–218.
[19] D.B. Clegg, R.L. Whitmore, Boundary layers in Bingham plastics, Rheol. Acta 5 (2) (1966) 130–134.
[20] J. Boujlel, M. Maillard, A. Lindner, G. Ovarlez, X. Chateau, P. Coussot, Boundary layer in pastes—Displacement of a long object through a yield stress fluid, J. Rheol. 56 (5) (2012) 1083–1108.
[21] F. Ahonguio, L. Jossic, A. Magnin, F. Dufour, Flow of an elasto-viscoplastic fluid around a flat plate: Experimental and numerical data, J. Non-Newton. Fluid Mech. 238 (2016) 131–139.
[22] J.-M. Piau, K. Debiane, The adhesive or slippery flat plate viscoplastic boundary layer for a shear-thinning power-law viscosity, J. Non-Newton. Fluid Mech. 117 (2–3) (2004) 97–107.
[23] E. Chaparian, I.A. Frigaard, Yield limit analysis of particle motion in a yield-stress fluid, J. Fluid Mech. 819 (2017) 311.
[24] P. Mosolov, V. Miasnikov, Variational methods in the theory of the fluidity of a viscous-plastic medium, J. Appl. Math. Mech. 29 (3) (1965) 545–577.
[25] P. Szabo, O. Hassager, Flow of viscoplastic fluids in eccentric annular geometries, J. Non-Newton. Fluid Mech. 45 (2) (1992) 149–169.
[26] P. Saramito, N. Roquet, An adaptive finite element method for viscoplastic fluid flows in pipes, Comput. Methods Appl. Mech. Engrg. 190 (40–41) (2001) 5391–5412.
[27] O.F. Meuric, R.J. Wakeman, T.W. Chiu, K.A. Fisher, Numerical flow simulation of viscoplastic fluids in annuli, Can. J. Chem. Eng. 76 (1) (1998) 27–40.
[28] M.A. Moyers-Gonzalez, I.A. Frigaard, Numerical solution of duct flows of multiple visco-plastic fluids, J. Non-Newton. Fluid Mech. 122 (1–3) (2004) 227–241.
[29] R.R. Huilgol, A systematic procedure to determine the minimum pressure gradient required for the flow of viscoplastic fluids in pipes of symmetric cross-section, J. Non-Newton. Fluid Mech. 136 (2–3) (2006) 140–146.
[30] A. Wachs, Numerical simulation of steady bingham flow through an eccentric annular cross-section by distributed Lagrange multiplier/fictitious domain and augmented Lagrangian methods, J. Non-Newton. Fluid Mech. 142 (1–3) (2007) 183–198.
[31] E.A. Muravleva, L.V. Muravleva, Unsteady flows of a viscoplastic medium in channels, Mech. Solids 44 (5) (2009) 792.
[32] M.F. Letelier, D.A. Siginer, C.B. Hinojosa, On the physics of viscoplastic fluid flow in non-circular tubes, Int. J. Non-Linear Mech. 88 (2017) 1–10.
[33] E. Chaparian, I.A. Frigaard, Cloaking: Particles in a yield-stress fluid, J. Non-Newton. Fluid Mech. 243 (2017) 47–55.
[34] E. Chaparian, A. Wachs, I.A. Frigaard, Inline motion and hydrodynamic interaction of 2D particles in a viscoplastic fluid, Phys. Fluids 30 (3) (2018) 033101.
[35] E. Comparini, E. De Angels, Flow of a Bingham fluid in a concentric cylinder viscometer, Adv. Math. Sci. Appl. 6 (1996) 97–116.
[36] K. Sekimoto, An exact non-stationary solution of simple shear flow in a Bingham fluid, J. Non-Newton. Fluid Mech. 39 (1) (1991) 107–113.
[37] K. Sekimoto, Motion of the yield surface in a Bingham fluid with a simple-shear flow geometry, J. Non-Newton. Fluid Mech. 46 (2–3) (1993) 219–227.
[38] R.R. Huilgol, On kinematic conditions affecting the existence and non-existence of a moving yield surface in unsteady unidirectional flows of Bingham fluids, J. Non-Newton. Fluid Mech. 123 (2–3) (2004) 215–221.
[39] N.J. Balmforth, Y. Forterre, O. Pouliquen, The viscoplastic Stokes layer, J. Non-Newton. Fluid Mech. 158 (1–3) (2009) 46–53.
[40] I.-C. Chan, P.L. Liu, Responses of Bingham-plastic muddy seabed to a surface solitary wave, J. Fluid Mech. 618 (2009) 155.

[41] Y.S. Park, P.L. Liu, Oscillatory pipe flows of a yield-stress fluid, J. Fluid Mech. 658 (2010) 211.

[42] L. Lacaze, A. Filella, O. Thual, Steady and unsteady shear flows of a viscoplastic fluid in a cylindrical couette cell, J. Non-Newton. Fluid Mech. 220 (2015) 126–136.

[43] V.M. Entov, Analogy between equations of plane filtration and equations of longitudinal shear of nonlinearly elastic and plastic solids, J. Appl. Math. Mech. 34 (1) (1970) 153–164.

[44] R. Goldstein, V.M. Entov, Qualitative Methods in Continuum Mechanics, Longman Scientific and Technical: Pitman Monographs and Surveys in Pure and Applied Mathematics 72, 1994.

[45] C. Atkinson, K. El-Ali, Some boundary value problems for the Bingham model, J. Non-Newton. Fluid Mech. 41 (3) (1992) 339–363.

[46] R.V. Craster, Solutions for Herschel-Bulkley flows, Quart. J. Mech. Appl. Math. 48 (4) (1995) 343–374.

[47] R.V. Craster, Yield surfaces for Herschel-Bulkley flows in complex geometries, IMA J. Appl. Math. 56 (3) (1996) 253–276.

[48] D.R. Hewitt, M. Daneshi, N.J. Balmforth, D. Martinez, Obstructed and channelized viscoplastic flow in a Hele–Shaw cell, J. Fluid Mech. 790 (2016) 173–204.

[49] V.M. Entov, T.A. Malakhova, Filtration problems with a piecewise-linear resistance law, Fluid Dyn. 9 (2) (1974) 194–198.

[50] N.K. Basak, G.A. Dombrovskii, A law of filtration with limiting gradient, Fluid Dyn. 18 (3) (1983) 404–406.

[51] N.K. Basak, G.A. Dombrovskii, Solution of a problem of flow in a porous medium with limiting gradient, Fluid Dyn. 20 (1) (1985) 66–68.

[52] G.A. Dombrovskii, On some special laws of non-linear filtration, J. Appl. Math. Mech. 52 (4) (1988) 533–536.

[53] C.W. Boast, P. Baveye, Solution of the flow at a corner problem with a stagnation zone, Water Resour. Res. 25 (4) (1989) 757–763.

[54] A.N. Alexandrou, V. Entov, On the steady-state advancement of fingers and bubbles in a Hele–Shaw cell filled by a non-Newtonian fluid, European J. Appl. Math. 8 (1) (1997) 73–87.

[55] A.N. Alexandrou, V.M. Entov, S.S. Kolganov, N.V. Kolganova, On bubble rising in a Hele-Shaw cell filled with a non-Newtonian fluid, European J. Appl. Math. 15 (3) (2004) 315.

[56] E.I. Anderson, Explicit solutions to two problems of steady groundwater flow with a threshold gradient, Water Resour. Res. 45 (2009) W02504.

[57] M.G. Alishaev, V.M. Entov, A.E. Segalov, Elementary solutions of plane nonlinear filtration problems, Fluid Dyn. 4 (3) (1969) 77–84.

[58] G. Brookes, R. Whitmore, Drag forces in Bingham plastics, Rheol. Acta 8 (4) (1969) 472–480.

[59] F. Savreux, P. Jay, A. Magnin, Flow normal to a flat plate of a viscoplastic fluid with inertia effects, AIChE J. 51 (3) (2005) 750–758.

[60] Z. Ouattara, P. Jay, A. Magnin, Flow of a Newtonian fluid and a yield stress fluid around a plate inclined at 45° in interaction with a wall, AIChE J. 65 (5) (2019) e16562.

[61] Z. Ouattara, A. Magnin, D. Blésès, P. Jay, Influence of the inclination of a plate on forces generated in flows of Newtonian and yield stress fluids, Chem. Eng. Sci. 197 (2019) 246–257.

[62] D.R. Hewitt, N.J. Balmforth, Viscoplastic slender-body theory, J. Fluid Mech. 856 (2018) 870–897.

[63] R. Glowinski, A. Wachs, On the numerical simulation of viscoplastic fluid flow, in: Handbook of Numerical Analysis, vol. 16, Elsevier, 2011, pp. 483–717.

[64] J. Bleyer, Advances in the simulation of viscoplastic fluid flows using interior-point methods, Comput. Methods Appl. Mech. Engrg. 330 (2018) 368–394.

[65] S.H. Bittleston, J. Ferguson, I.A. Frigaard, Mud removal and cement placement during primary cementing of an oil well–Laminar non-Newtonian displacements in an eccentric annular Hele-Shaw cell, J. Eng. Math. 43 (2–4) (2002) 229–253.

[66] N.J. Balmforth, Viscoplastic asymptotics and other analytical methods, in: Lectures on Visco-Plastic Fluid Mechanics, Springer, 2019, pp. 41–82.

[67] I.A. Frigaard, D.P. Ryan, Flow of a visco-plastic fluid in a channel of slowly varying width, J. Non-Newton. Fluid Mech. 123 (1) (2004) 67–83.

[68] Y. Liu, N.J. Balmforth, S. Hormozi, Viscoplastic surges down an incline, J. Non-Newton. Fluid Mech. 268 (2019) 1–11.